REVIEW

Check for updates

Carrier transport mechanisms in polycrystalline semiconductors: from grain boundary physics to device performance

Israt Jahan, [ID] Jesus Dustin Arellano [ID] and Zhisheng Shi [ID] *

Polycrystalline semiconductors are central to modern optoelectronic and energy devices, yet their performance is governed by the chemistry and electrostatics of grain boundaries (GBs). Unlike single crystals, polycrystalline systems exhibit potential barriers, trap states, and compositional inhomogeneities that critically shape carrier mobility, lifetime, and recombination. This review unifies theoretical and experimental perspectives on major transport pathways—drift–diffusion, thermionic emission, tunneling, hopping, and conduction through threading crystallites—across representative materials including Si, CdTe, CIGS, PbSe, Sb_2Se_3, Bi_2Te_3, Mg_3Sb_2, and halide perovskites. Particular emphasis is placed on how nanoscale probes such as Kelvin probe and conductive AFM, cathodoluminescence, and DLTS elucidate barrier heights, trap energetics, and boundary passivation effects. Chemical and structural strategies—such as halogen or alkali–fluoride treatments, dopant redistribution, anti-barrier engineering, and twin-boundary engineering—are demonstrated to transform recombination-active interfaces into conductive channels. By correlating microscopic boundary chemistry with macroscopic transport and device metrics, this review formulates general design guidelines for programmable grain architectures. The analysis establishes grain boundaries not as fixed defects but as tunable electronic interfaces, offering a roadmap for next-generation polycrystalline semiconductors optimized for high-mobility, high-stability optoelectronic and thermoelectric applications.

School of Electrical and Computer Engineering, University of Oklahoma, Norman, Ok 73019, USA. E-mail: Shi@ou.edu

Israt Jahan

Israt Jahan is a PhD candidate working in the Optoelectronics Laboratory at the University of Oklahoma, supervised by Dr Zhisheng Shi. Her research focuses on the growth, fabrication, and characterization of mid-infrared photodetectors based on polycrystalline lead chalcogenides grown by Molecular Beam Epitaxy and Chemical Bath Deposition. She specializes in device fabrication, sensitization optimization, and radiometric measurements, with emphasis on grain-boundary physics and charge-transport mechanisms. Her work integrates materials science, device engineering, and optoelectronic characterization to advance high-performance MWIR imaging technologies.

Jesus Dustin Arellano

Jesus Dustin Arellano is a current PhD candidate working in Dr Zhisheng Shi's lab at the University of Oklahoma on PbSe photoconductor devices with an emphasis on MBE growth and optimized sensitization of thin films. Another area of interest that he is focused on is understanding the noise analysis of these samples and comparing them to commercially available PbSe detectors with the goal of improving performance.

This journal is © The Royal Society of Chemistry 2025

J. Mater. Chem. C, 2025, **13**, 23675–23695 | **23675**

1 Introduction

Polycrystalline semiconductors are integral to a wide range of contemporary technologies, including electronics, optoelectronics, and energy conversion systems, owing to their cost-effective fabrication methods, tunable material properties, and compatibility with large-area deposition. In contrast to single-crystalline materials, which require precise and resource-intensive growth techniques, polycrystalline thin films can be fabricated *via* scalable approaches such as chemical vapor deposition (CVD), molecular beam epitaxy (MBE), and solution-based processes. These fabrication routes facilitate integration over flexible or inexpensive substrates.

Unlike single crystals, where the periodic and defect-minimized lattice enables smooth electronic band structures, characterized by flat conduction and valence bands that support unobstructed drift and diffusion of carriers with minimal scattering, polycrystalline materials are composed of many crystallites separated by grain boundaries (GBs). These boundaries often serve as reservoirs for electrically active defect states—frequently modelled as ionized donor- or acceptor-like traps—which can capture mobile carriers. The resultant accumulation of fixed charge at GBs induces electrostatic potential variations and leads to the formation of depletion or accumulation zones. These localized space-charge regions exhibit pronounced band bending, which in turn alters carrier transport pathways and contributes to the non-ideal electronic behaviour observed in polycrystalline films.[1–3]

The electrostatic band bending induced by grain boundaries (GBs) plays a pivotal role in modulating charge carrier transport. As schematically depicted in Fig. 1, energy bands in polycrystalline materials exhibit upward or downward bending near GBs, forming potential barriers that obstruct carrier motion. These barriers can reflect carriers, impose thermal repulsion, or enable quantum mechanical filtering depending on the carriers' energy distribution and the strength of local electric fields. The extent of the barrier is often quantified using the Seto model, which correlates the barrier height to doping concentration and trap state density at the boundary interface.[4] Such GB-induced potential profiles result in deviations from ideal drift–diffusion behaviour, promoting alternative transport mechanisms such as thermionic emission, field-enhanced tunneling, or hopping conduction—particularly at low temperatures or in defect-rich systems.

Nonetheless, through careful material and interface engineering, several polycrystalline systems have overcome these limitations and achieved state-of-the-art performance in practical devices. Polycrystalline metal halide perovskites, for instance, have rapidly emerged as leading photovoltaic materials, achieving power conversion efficiencies (PCEs) exceeding 24.8% and external quantum efficiencies (EQEs) up to 93%, rivaling those of single-crystal silicon devices.[7,8] These remarkable results are attributed to long carrier diffusion lengths, benign grain boundaries, and defect-tolerant electronic structures. Polycrystalline silicon (poly-Si) remains the dominant material in commercial solar panels, balancing cost, scalability, and efficiency, with laboratory-scale devices exceeding 22% PCE.[9] Likewise, cadmium selenide telluride (CST) and copper indium gallium selenide (CIGS) thin films have reached power conversion efficiencies above 22% and 23%, respectively, while offering compatibility with flexible or inexpensive substrates.[10,11] In the realm of infrared and broadband photodetection, semiconductors such as lead selenide (PbSe), antimony selenide (Sb_2Se_3), tin sulphide (SnS), and lead sulphide (PbS) have emerged as promising candidates due to their tunable bandgaps and intrinsic tolerance to defects.[12–15] These materials support long carrier lifetimes and stable performance even in the presence of high defect densities—an essential feature for mid-wave infrared (MWIR) and near-infrared sensing technologies.

Polycrystalline materials are also central to thermoelectric applications, where compounds such as bismuth telluride (Bi_2Te_3), lead telluride (PbTe), and half-Heusler alloys benefit from microstructural engineering strategies that selectively suppress lattice thermal conductivity while maintaining or enhancing electronic transport. This decoupling effect leads to improved thermoelectric figure of merit (ZT).[16] Recently, n-type $Mg_3(Sb,Bi)_2$ has drawn considerable attention as a high-performance thermoelectric material, achieving a record peak ZT of ~ 2.0 and an average ZT above 1.5 through interfacial and grain-boundary engineering.[17] Furthermore, polycrystalline n-type metal oxides, including tin dioxide (SnO_2) and zinc oxide (ZnO), are widely deployed in gas sensors, where carrier concentration at grain boundaries (GBs) is modulated by adsorbed gas species, yielding high chemical sensitivity.[18] In thin-film transistor (TFT) applications, particularly for display backplanes and flexible electronics, polycrystalline silicon (poly-Si) remains the material of choice despite the adverse effects of grain-induced scattering. Its compatibility with established silicon processing and favourable mechanical properties ensures continued relevance in logic and active-matrix circuits.[19]

Among the various microstructural features in polycrystalline semiconductors, twin boundaries (TBs) stand out as a

Zhisheng Shi received his PhD in opto-electronic materials in 1995 from Physics Department in Albert-Ludwig-University in Freiburg, Germany. His PhD research work was performed at Fraunhofer Institute (FhG) for Physical Measurement Techniques (IpM). From 1995 to 1997, he was a research staff at Swiss Federal Institute of Technology (ETH). He has been a faculty member in the School of Electrical and Computer engineering at the University of Oklahoma (OU) since 1997. Dr Shi's research includes mid-wave infrared (MWIR) detectors, semiconductor photovoltaic solar cells, and mid-IR lasers and LEDs.
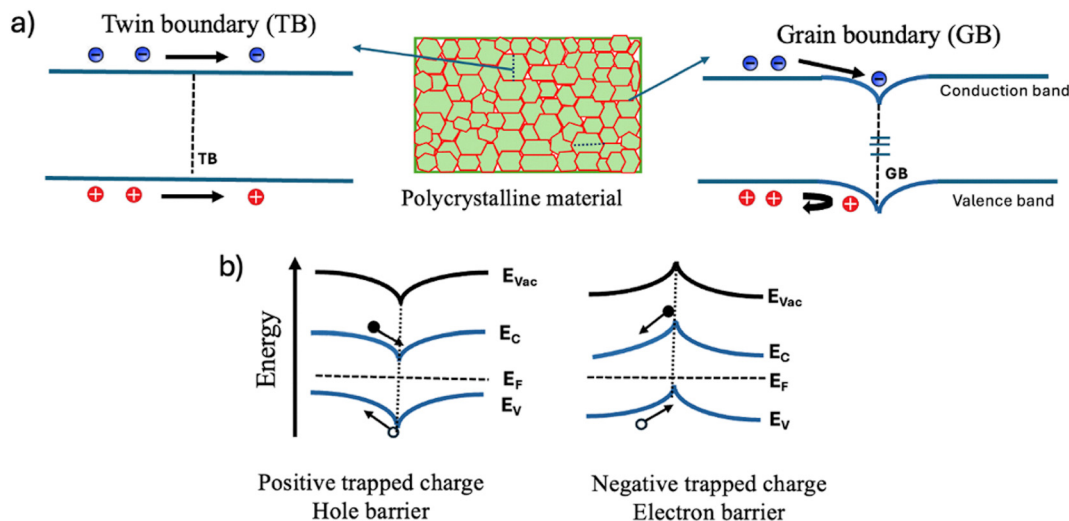
Zhisheng Shi

Fig. 1 Schematic band diagrams illustrating the impact of grain and twin boundaries on carrier transport. (a) Energy diagrams comparing GBs and twin boundaries (TBs): GBs act as recombination-active regions with band bending and carrier trapping, while TBs, owing to their symmetry and low defect density, provide recombination-free, conductive pathways. Adapted from Xun Xiao *et al.*, *Nat. Commun.*, 2020, **11**, 2215. https://doi.org/10.1038/s41467-020-16075-1. Licensed under CC BY 4.0 (https://creativecommons.org/licenses/by/4.0/).[5] (b) Grain boundaries (GBs) can introduce hole barriers (left), electron barriers (right), impeding carrier mobility, Adapted from Nicoleta Nicoara *et al.*, *Nat. Commun.*, 2019, **10**, 3980. Licensed under CC BY 4.0 (https://creativecommons.org/licenses/by/4.0/).[6]

unique class of planar defects. Unlike conventional grain boundaries, TBs typically possess low defect densities and do not substantially disturb the periodic potential landscape. As a result, they rarely introduce deep-level trap states or significant band bending. In fact, TBs have been reported to facilitate directional carrier transport along specific lattice axes and may enhance overall electronic performance. In materials such as CdTe, TBs have been associated with efficient carrier collection and are increasingly regarded as electronically benign or even performance-enhancing features.[2,20,21]

Understanding the interplay between microstructure and charge transport is essential for advancing the performance of polycrystalline devices. This review presents an integrative analysis of charge transport mechanisms in polycrystalline semiconductors, encompassing theoretical models and experimental observations. Topics covered include major conduction mechanisms (*e.g.*, drift–diffusion, thermionic emission, tunneling, and hopping), the roles of GBs and TBs, and the effects of structural and electrical heterogeneities. By linking microscopic defect structures to macroscopic transport behavior, this work aims to inform design strategies for high-performance polycrystalline semiconductors in photovoltaic, optoelectronic, and thermoelectric applications.

2 Fundamentals of charge carrier transport

A fundamental understanding of charge carrier transport mechanisms is pivotal for the rational design and performance enhancement of semiconductor devices. In polycrystalline semiconductors, the dominant transport phenomena are carrier drift and diffusion, which govern movement in response to applied electric fields and concentration gradients, respectively. While these mechanisms form the basis of classical semiconductor transport theory, the presence of grain boundaries (GBs) in polycrystalline systems introduces spatial inhomogeneities and electrostatic discontinuities that complicate this otherwise idealized behavior. GBs act as scattering centers and potential barriers, disrupting the continuity of carrier flow and altering the local field distribution, thereby significantly influencing both drift- and diffusion-driven transport.

2.1 Drift and diffusion transport

The Charge carrier motion in semiconductors is fundamentally governed by two classical mechanisms: drift, driven by electric fields, and diffusion, arising from concentration gradients.[22] When an external electric field E is applied, electrons and holes experience an electric field force that induces a net directional movement, resulting in a drift current. The average carrier velocity under the field, or drift velocity, v_d, is given by:

$$v_d = \mu E \tag{1}$$

where μ is the mobility of the charge carriers, reflecting their ease of movement under an applied field. The drift current density J_{drift} can be expressed as:

$$J_{drift} = qn\mu E \tag{2}$$

With q representing the elementary charge and n the carrier concentration.[4] In single-crystal semiconductors, mobility is typically limited by phonon scattering and ionized impurity interactions.[22] However, in polycrystalline semiconductors, grain boundaries (GBs) introduce additional scattering and trapping centers that degrade carrier mobility. GBs act as electrostatic barriers, altering the local potential landscape

This journal is © The Royal Society of Chemistry 2025

J. Mater. Chem. C, 2025, **13**, 23675–23695 | **23677**

and impeding charge flow. One of the earliest models to quantify this effect was proposed by Seto, who attributed mobility degradation to potential barriers formed at GBs due to trapped interface charges. These trapped charges induce band bending at the grain interfaces, resulting in a thermally activated transport behavior—particularly significant in low-doped polycrystalline silicon films.[4] Expanding on this idea, Kim et al. developed a detailed drift–diffusion model treating GBs as amorphous regions in thermodynamic equilibrium with adjacent grains.[23] Their model successfully captures both small-signal behavior and nonlinear large-signal responses in polysilicon thin films, making it broadly applicable to thin-film devices such as thin-film transistors (TFTs).

Parallel to drift, carrier motion also occurs via diffusion, a thermally induced process where particles migrate from regions of high concentration to low concentration. The diffusion current density is described by,

$$J_{\text{Diffusion}} = qD\frac{\mathrm{d}x}{\mathrm{d}n} \tag{3}$$

where D is the diffusion coefficient and $\mathrm{d}x/\mathrm{d}n$ is the carrier concentration gradient. The Einstein relation links diffusion and mobility under conditions of thermal equilibrium:

$$D = \mu\frac{KT}{q} \tag{4}$$

Grain boundaries influence diffusion through two mechanisms: (1) they serve as energetic barriers hindering carrier transport, and (2) they provide fast-diffusion pathways for atomic species such as dopants and impurities.[2,22] For instance, Hwang et al. showed via Auger electron spectroscopy that aluminium diffuses preferentially along GBs in polycrystalline silicon—contrasting sharply with its limited bulk diffusivity.[24] This phenomenon plays a crucial role in the activation and redistribution of dopants during thermal processing steps.

To model such effects, Ling et al. proposed a diffusion-based model that incorporates GB-induced potential barriers.[25] By solving the carrier continuity equation across the GB depletion region, they demonstrated how variations in grain size and barrier height influence effective diffusion currents and lateral mobility. Complementing this, Santonen et al. examined how grain size distributions affect macroscopic drift–diffusion transport.[26] Their simulations revealed that broader grain size distributions reduce overall resistivity by enabling percolative pathways through low-barrier grains, effectively minimizing the number of transport-limiting junctions.

Beyond influencing carrier mobility and diffusion coefficients, GBs critically shape the local energy landscape. Electrostatic band bending at GBs results in potential barriers that carriers must overcome via thermionic emission or quantum tunneling—particularly at low temperatures or when barriers are high.[27] Accurately capturing these behaviors requires incorporating position-dependent mobility, spatially varying potential profiles, and non-uniform carrier distributions into device models.

To address these complexities, multiple extensions of the Seto model have been developed,[4] incorporating phenomena such as field-assisted tunneling, trap occupancy statistics, and nonlinear transport regimes. These enhancements are especially relevant for advanced polycrystalline devices, including photodetectors, TFTs, and thin-film solar cells.[28] Consequently, conventional drift–diffusion frameworks must be supplemented with grain-level and statistical descriptors, including grain size, trap density, and potential inhomogeneity. A comprehensive understanding of GB-driven transport is thus indispensable for predictive modeling and performance optimization of next-generation polycrystalline electronic and optoelectronic systems.

Taken together, these studies confirm that drift–diffusion transport in polycrystalline semiconductors cannot be described by classical models alone but must explicitly account for the electrostatics and chemistry of grain boundaries. Trap-induced band bending, dopant segregation, and impurity incorporation all redefine effective mobility and diffusion pathways, shifting transport away from ideal single-crystal behavior.[4,22–27] Importantly, GBs act not only as barriers but also as fast-diffusion conduits for impurities, making their chemical composition as decisive as their geometry in determining device performance. Extensions of the Seto model that incorporate field-assisted tunneling, trap statistics, and grain-size distributions demonstrate that predictive transport modeling requires grain-level descriptors rather than bulk averages.[4,26,28] Thus, drift–diffusion in polycrystalline systems reflects a balance between classical band transport and boundary-limited conduction, highlighting that controlling GB chemistry, trap density, and orientation is as essential as scaling grain size for optimizing electronic and optoelectronic devices.

2.2 Scattering mechanisms

The carrier transport in polycrystalline semiconductors is influenced by various scattering mechanisms, including phonon scattering, ionized impurity scattering, and grain boundary scattering. These mechanisms collectively determine the effective carrier mobility μ_{eff}, often represented by Matthiessen's rule:

$$\frac{1}{\mu_{\text{eff}}} = \frac{1}{\mu_{\text{ph}}} + \frac{1}{\mu_{\text{ii}}} + \frac{1}{\mu_{\text{GB}}} \tag{5}$$

where μ_{ph}, μ_{ii}, and μ_{GB} correspond to mobilities limited by phonon scattering, ionized impurity scattering, and grain boundary scattering, respectively.[29,30]

Phonon scattering arises from interactions between charge carriers and lattice vibrations. In polycrystalline materials, grain boundaries introduce additional phonon scattering centers, significantly reducing thermal conductivity (Fig. 2d). For instance, studies have shown that when phonons travel across grain boundaries, the rapidly changing strain fields can induce strong phonon scattering, leading to increased interfacial thermal resistance.[31] The temperature dependence of phonon-limited mobility is often expressed as: $\mu_{\text{ph}} \propto T^{-\gamma}$, where γ

23678 | J. Mater. Chem. C, 2025, **13**, 23675–23695

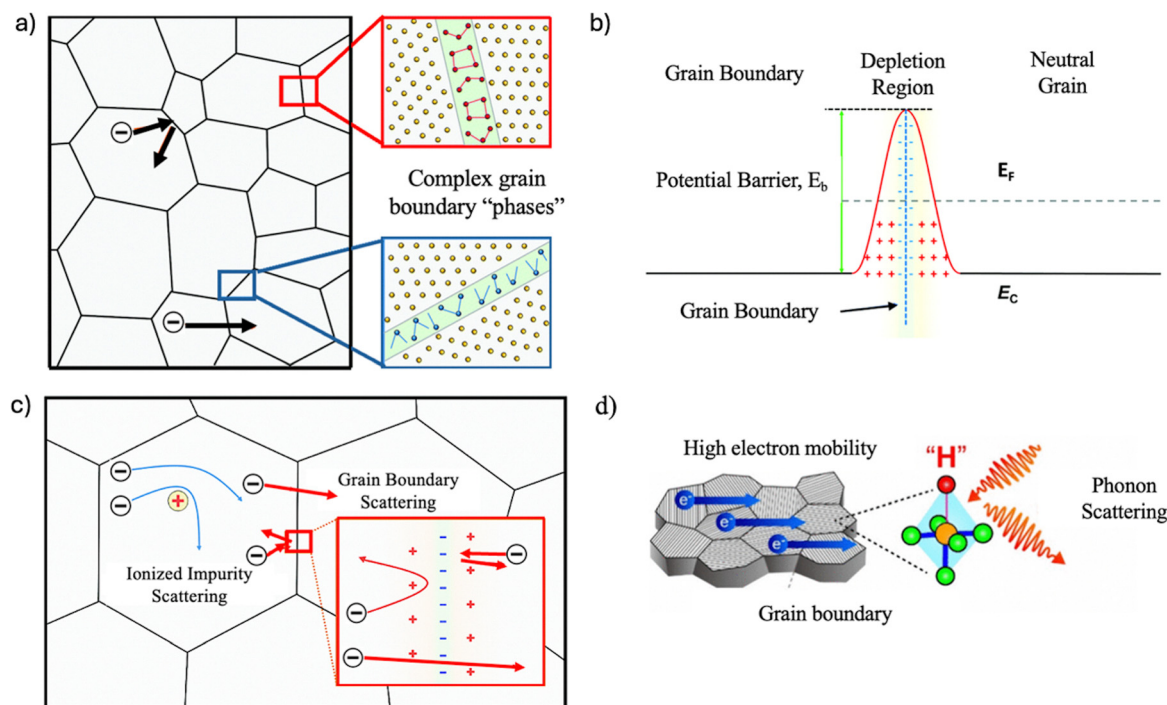This journal is © The Royal Society of Chemistry 2025

Fig. 2 Schematic illustration of scattering and energy landscape in polycrystalline semiconductors. (a) Structural complexity of grain boundaries (GBs), showing multiple phases and defect-rich regions. (b) Energy band diagram for an n-type polycrystalline material, where charged GB trap states induce band bending and depletion regions. (c) Representation of dominant scattering mechanisms, including ionized impurity scattering and grain boundary scattering. (a)–(c) are adapted from Chaoliang Hu *et al.*, *Energy Environ. Sci.*, 2021, **15**, 1406–1422, with permission from the Royal Society of Chemistry.[92] (d) Phonon scattering process affecting charge transport in polycrystalline $SrTiO_{3-x}H_x$. Adapted with permission from Takayoshi Katase *et al.*, *ACS Appl. Electron. Mater.*, 2024, **6** (10). Copyright 2024 American Chemical Society.[42]

typically ranges from 1.5 to 2.5, depending on the material and specific phonon interactions. This relationship indicates that as temperature increases, phonon scattering becomes more significant, leading to a decrease in carrier mobility.[32] Recent advancements have highlighted the role of strain fields induced by grain boundaries in enhancing phonon scattering. For example, in polycrystalline graphene, grain-boundary-induced strain fields have been identified as a decisive factor in electron scattering, affecting the material's electrical resistivity. Additionally, in materials like In_2Te_3, strong phonon scattering on point defects has been observed, contributing to low thermal conductivity.[33–35]

Ionized impurity scattering (IIS) occurs when charge carriers interact with ionized dopants within the semiconductor (Fig. 2c). This mechanism is particularly significant in heavily doped polycrystalline films, where the Coulombic interactions between carriers and charged impurities can substantially impede carrier mobility. The mobility limited by ionized impurity scattering is inversely related to the impurity concentration and exhibits a temperature dependence that varies based on screening effects and carrier concentration.[27,36] In highly doped polycrystalline semiconductors, such as aluminium-doped zinc oxide (AZO), ionized impurity scattering becomes a dominant factor affecting electron transport. Studies have shown that at high doping levels, the net charge of ionized impurities leads to Coulomb potentials, which constitute significant scattering centers for charge carriers. Furthermore, in

materials like zinc tin oxide (ZTO), both ionized impurity and grain boundary scattering mechanisms have been identified as temperature-independent factors limiting electron mobility.[37] Advancements in first-principles calculations have enabled more accurate predictions of carrier scattering rates due to ionized impurities. These computational methods have been applied to various semiconductors, providing insights into the impact of ionized impurity scattering on electronic transport properties.[38] Recent work on n-type $Mg_3(Sb,Bi)_2$ crystallizes how the balance among ionized-impurity scattering and grain-boundary (GB) barriers determines low-temperature transport. Shuai *et al.*[39] showed that modest Nb co-doping converts the dominant scattering from IIS to a mixed IIS + acoustic-phonon regime, thereby tripling the power factor and increasing Hall mobility from ~ 19 to ~ 77 $cm^2\,V^{-1}\,s^{-1}$ through dielectric screening-driven IIS suppression. This study suggests that reducing IIS (intragrain) and lowering GB barrier resistance (intergrain) are orthogonal knobs for mobility engineering in polycrystals.

Grain boundaries in polycrystalline semiconductors serve as potential barriers to charge carriers, resulting in scattering and trapping phenomena that degrade electrical performance (Fig. 2c). The impact of grain boundary scattering on carrier mobility can be described by,

$$\mu_{GB} \propto e^{-\frac{E_B}{KT}} \qquad (6)$$

This journal is © The Royal Society of Chemistry 2025

J. Mater. Chem. C, 2025, **13**, 23675–23695 | **23679**

where E_B is the grain boundary barrier height, K is the Boltzmann constant, and T is the temperature. This expression indicates that grain boundary scattering has a thermally activated behavior, with mobility decreasing as the barrier height increases.[4,27] Recent studies have demonstrated that engineering grain boundaries can mitigate scattering effects and enhance carrier mobility in polycrystalline semiconductors. For example, in organic semiconductor films, grain boundary engineering through controlled deposition techniques has been shown to improve electrical performance by reducing trap densities and potential barriers at grain boundaries.[40] Furthermore, advanced characterization techniques, such as scanning transmission electron microscopy (STEM), have provided deeper insights into the atomic structure and chemistry of grain boundaries. These studies have revealed the presence of localized strain fields and defect states at grain boundaries, which significantly influence carrier scattering mechanisms.[41]

In summary, scattering mechanisms in polycrystalline semiconductors reflect the combined influence of lattice dynamics, impurity distribution, and grain boundary chemistry. Phonon scattering dominates at elevated temperatures, ionized impurity scattering prevails in heavily doped regimes, and grain boundary scattering governs mobility in low-doped or trap-rich systems.[4,27,29–32,36–38,42] A unifying theme across these regimes is that grain boundaries act as chemically active scattering centers, where strain fields, dopant segregation, and localized defects enhance phonon and Coulombic scattering in ways that bulk models cannot capture.[33–35,40,41] Importantly, evidence from organic semiconductors and oxide films shows that grain boundary engineering—through deposition control, passivation, and chemical doping—can mitigate these effects by lowering trap densities and redistributing impurities.[37,40,41] These findings emphasize that scattering in polycrystalline semiconductors is not solely a structural phenomenon but a chemistry-governed process, highlighting the importance of defect chemistry and boundary treatments as decisive levers for optimizing carrier mobility.

2.3 Carrier lifetime and recombination

The Carrier lifetime—the average time a photogenerated or injected carrier remains mobile before recombination—is a pivotal parameter governing the performance of optoelectronic and photovoltaic devices. In polycrystalline semiconductors, this lifetime is significantly influenced by intrinsic material properties such as grain boundaries (GBs), dislocations, and trap states, which introduce additional non-radiative recombination pathways absent in single-crystalline counterparts. The total carrier lifetime (τ_{eff}) in polycrystalline materials is determined by the combined effects of bulk (grain interior) recombination and recombination at GBs. It is commonly expressed as:

$$\frac{1}{\tau_{eff}} = \frac{1}{\tau_{bulk}} + \frac{1}{\tau_{GB}} \tag{7}$$

where τ_{bulk} is the lifetime within grains and τ_{GB} is the effective recombination time due to grain boundaries. Grain boundaries

can harbor a high density of defect states that serve as efficient recombination centers, dramatically reducing τ_{eff}.[43]

The dominant recombination mechanisms in semiconductors are: (i) radiative recombination, where electrons and holes recombine to emit photons; (ii) Auger recombination, involving a third carrier that absorbs the recombination energy; and (iii) Shockley–Read–Hall (SRH) recombination, which occurs *via* trap states within the bandgap. In high-quality single crystals, radiative recombination may dominate under high injection, but in polycrystalline films, SRH recombination is often the primary non-radiative pathway due to a high density of trap states near GBs.[44] The SRH recombination rate is given by:

$$R_{SRH} = \frac{np - n_i^2}{\tau_p(n + n_1) + \tau_n(p + p_1)} \tag{8}$$

where τ_n and τ_p are the electron and hole lifetimes, and n_1, p_1 are related to the energy level of the trap.[22] In $Cu(In,Ga)Se_2$ thin films, GB recombination velocities as high as 10^3 cm s^{-1} have been reported, severely limiting open-circuit voltage and minority carrier diffusion lengths.[45] Similarly, in poly-Si and CdTe, deep-level traps associated with extended defects dominate SRH-type recombination.[46]

Grain boundaries are known to introduce defect states that trap carriers and create local band bending. This band bending separates quasi-Fermi levels, enhances recombination, and can substantially reduce effective diffusion lengths. According to Gaury and Haney, the recombination activity of GBs depends on their charge state and the type of traps present. For instance, a single donor state at the GB can dramatically suppress recombination relative to donor–acceptor continua. Experimental studies using cathodoluminescence and electron-beam-induced current (EBIC) have confirmed that GBs can either serve as recombination sinks or quasi-passive interfaces, depending on their chemical and electrical character.[43,47]

Carrier lifetime in polycrystalline materials is often measured using time-resolved photoluminescence (TRPL). Modern halide perovskites exhibit lifetimes exceeding 6 μs—approaching values observed in single crystals—due to intrinsic defect tolerance and high GB passivation.[48] However, lifetime measurements are frequently complicated by spatial inhomogeneities caused by variation in trap density across grains and GBs. In surface-limited recombination scenarios, the lifetime can be expressed empirically as:

$$\tau_{eff} = \frac{d}{2S} \tag{9}$$

where d is the grain size and S is the surface recombination velocity at GBs.[22] This scaling suggests that increasing grain size or reducing GB recombination velocity *via* passivation can significantly enhance device performance.

Collectively, these findings demonstrate that carrier lifetime in polycrystalline semiconductors is dictated not simply by bulk recombination but by the chemical nature and charge state of grain boundaries. While SRH recombination dominates in trap-rich systems such as poly-Si, CdTe, and CIGS.[43–46] Halide perovskites illustrate that benign or passivated boundaries can

23680 | *J. Mater. Chem. C*, 2025, **13**, 23675–23695

This journal is © The Royal Society of Chemistry 2025

yield lifetimes approaching those of single crystals.[48] Microscopy studies further confirm that GBs may behave as either recombination sinks or quasi-passive interfaces, depending on their defect chemistry and electrostatics.[43,47] This duality underscores the central role of boundary chemistry, defect passivation, and grain size control in governing τ_{eff}, with strategies such as Cl/Cu passivation in CdTe or compositional engineering in perovskites providing clear pathways to extend carrier lifetimes.[46–48] Thus, lifetime engineering in polycrystalline semiconductors is less a matter of eliminating GBs and more about chemically tuning their recombination activity, establishing GB chemistry as a decisive design parameter for next-generation optoelectronic and photovoltaic devices.

3 Major conduction mechanisms

3.1 Thermionic emission across grain boundaries

3.1.1 Theoretical background. Thermionic emission is a well-established mechanism describing charge carrier transport across potential barriers at grain boundaries (GBs) in polycrystalline semiconductors. Recent studies continue to refine our understanding of GB-limited transport, particularly in optoelectronic and thermoelectric materials where GB engineering plays a decisive role in performance tuning.[49] Originally introduced by Seto,[4] this model treats GBs as electrostatic potential barriers formed due to the presence of charged trap states at the interfaces between adjacent grains. These trapped charges distort the local electrostatic potential, inducing band bending and forming depletion regions within the neighbouring grain interiors. Recent studies have shown that depletion widths at GBs vary substantially depending on compositional heterogeneity, post-deposition annealing, and impurity segregation, resulting in highly non-uniform electrostatic profiles.[50] Under conditions of moderate doping and elevated temperature, free carriers—electrons in n-type or holes in p-type materials—can acquire sufficient thermal energy to overcome these electrostatic barriers. This process gives rise to a current that can be described by the Richardson–Schottky thermionic emission equation:

$$J = A \times T^2 e^{\frac{-q\varphi_{\text{B}}}{KT}} \qquad (10)$$

where J is the current density across GB, $A^\star$ is the Richardson constant, and φ_{B} is the barrier height.[51] Unlike Schottky barriers at metal–semiconductor interfaces, the grain boundary barrier height is extrinsic and governed by trap state density (N_{t}) and carrier concentration (n). An approximate expression for φ_{B}, assuming a one-dimensional depletion approximation, is given by:

$$\varphi_{\text{B}} = \frac{q^2 N_{\text{t}}^2}{8\varepsilon\varepsilon_0 n} \qquad (11)$$

This expression illustrates that a high density of trap states or a low carrier concentration results in an increased barrier height, thereby suppressing conduction.[4,22,50] Consequently, the mobility of charge carriers in such GB-limited

systems follows an Arrhenius-type temperature dependence: $\mu(T) \propto e^{\frac{-\varphi_{\text{B}}}{KT}}$. This exponential dependence has been widely observed in experiments involving temperature-dependent Hall measurements and photoconductivity studies.[49,52] It reflects the thermally activated nature of carrier transport across the grain boundaries. Furthermore, the influence of grain structure becomes evident when considering the total resistance of a polycrystalline film. If a material is composed of grains of average size d, the total device resistance scales with the number of boundaries per unit length:

$$R_{\text{Total}} \propto \frac{L}{d} e^{\frac{-\varphi_{\text{B}}}{KT}} \qquad (12)$$

This relationship highlights key material design strategies: increasing grain size, reducing GB trap density, or enhancing carrier concentration will all serve to lower the effective resistance and improve conductivity. While Seto's model provides a foundational understanding, more recent theoretical developments have refined this picture by incorporating the effects of barrier height fluctuation, partial depletion, and image-force lowering, and non-uniform spatial distributions of trap states, which more accurately reflect the complexities of real grain boundaries in modern semiconductor materials.[49,51,53]

3.1.2 Microscopic and experimental evidence of thermionic emission at GBs. Thermionic emission across grain boundaries (GBs) has been extensively validated in polycrystalline semiconductors through a combination of temperature-dependent transport measurements, microscopic imaging techniques, and device-level modeling. A consistent observation across various material systems is the Arrhenius-type increase in conductivity or mobility within intermediate temperature regimes (typically 150–350 K), which aligns well with activation energies predicted by the Seto model of thermally assisted barrier-limited transport.[4,49,50,52]

In polycrystalline CuGaSe$_2$, Schuler et al. identified three distinct conduction regimes via Hall measurements from 80 to 350 K. Notably, the intermediate regime (150–300 K) exhibited mobility activation energies ranging between 60 and 135 meV, consistent with thermionic emission across GB barriers.[27] Similarly, Cifuentes et al. reported thermionic emission as the dominant transport mechanism in Sb$_2$Se$_3$ thin films above 200 K, with conductivity fits yielding barrier heights of approximately 391 meV and trap densities on the order of 3.4×10^{11} cm^{-2}.[54] In ZnO-based systems, doping levels were found to govern the dominant transport mode. Kajikawa et al. observed that moderately doped Al:ZnO ($\sim 10^{18}$ cm^{-3}) films displayed thermionic emission-limited conduction with GB barriers between 70–120 meV.[50] However, at higher doping levels exceeding 10^{19} cm^{-3}, tunneling mechanisms began to dominate due to the narrowing of depletion regions.

In elemental polycrystalline semiconductors such as silicon, Lu et al. proposed a conduction model based on sequential semiconductor–grain-boundary–semiconductor (S–GB–S) barriers. Their experimental studies in thermally grown poly-Si revealed that thermionic emission dominated charge transport,

This journal is © The Royal Society of Chemistry 2025

J. Mater. Chem. C, 2025, **13**, 23675–23695 | **23681**

with conduction scaling determined by grain size, dopant density, and GB trap states.[51] Similar effects were described in polycrystalline PbS, where Slater developed a GB barrier model to explain temperature-activated photoconductivity. Activation energies up to 370 meV were found, depending on oxidation and microstructure, confirming that GB-induced potential barriers critically influence dark conductivity and its temperature dependence.[55]

Beyond macroscopic transport studies, direct nanoscale imaging techniques have provided microscopic confirmation of GB barriers and electrostatic potential modulation. In NiO thin films, Zhang *et al.* employed conductive atomic force microscopy (C-AFM) and Kelvin probe force microscopy (KPFM) to spatially map local current distribution and surface potential across grains and boundaries. Their measurements revealed nanoscale potential differences of $\sim$17–23 meV at GBs, and *I–V* curves indicative of thermionic emission behavior. These results confirmed the existence of energy barriers that modulate local carrier flow in polycrystalline NiO (Fig. 3(d–f)).[56]

Such nanoscale measurements are consistent with macroscopic device performance in halide perovskites. KPFM studies of MAPbI$_3$ films reported by Bahrami *et al.* showed GB potential barriers between 20 and 43 meV, depending on humidity exposure. The presence of these electrostatic barriers limited carrier collection and exhibited thermal activation consistent with the Richardson–Schottky model of thermionic transport.[57] Yun *et al.* further demonstrated that GBs serve as preferential paths for ion migration and recombination, supporting the idea that GBs are electrostatically active sites influencing charge separation and transport.[58]

The importance of GB electrostatics has also been validated using electron beam induced current (EBIC) imaging. In polycrystalline CdTe/CdS solar cells, Li *et al.* observed that untreated GBs appeared as dark features in EBIC maps due to poor collection efficiency. Post-CdCl$_2$ treatment, however, these same GBs exhibited bright contrast, indicative of enhanced local collection driven by GB-induced band bending (Fig. 3g). The activation was attributed to a CdCl$_2$-induced p-to-n type inversion at GBs that created internal fields enhancing thermionic carrier separation.[59,60] These findings are consistent with first-principles calculations by Zhang *et al.*, who showed that Cl and Cu preferentially accumulate at Te-core GBs in CdTe. Without copassivation, these boundaries host deep states near the conduction band minimum; combined Cl–Cu treatment effectively removes these levels, validating the electrostatic origin of GB barriers.[61]

Further insights have been gained through optoelectronic characterization techniques such as time-resolved photoluminescence (TRPL) and infrared light-beam induced current (IR-LBIC) mapping. In Cs-doped FAPbI$_3$ thin films, Ma *et al.* showed that grain boundaries exhibited slightly reduced diffusion lengths (3–5 µm) and enhanced charge trapping compared to grain interiors. Despite long carrier lifetimes overall, the observed spatial heterogeneity in photoconductivity supports the presence of weak GB barriers that contribute to thermally activated transport under certain conditions.[62]

A clear manifestation of thermionic emission–limited charge transport has been observed in n-type Mg$_3$Sb$_2$-based thermoelectric materials, which display thermally activated carrier mobility below approximately 500 K. Kuo *et al.*[63] explained this behavior using a two-phase grain/grain-boundary transport model, in which depletion layers at the grain boundaries create potential barriers of about 60 meV. Electrons must surmount these barriers to contribute to conduction, giving rise to the characteristic Arrhenius-type temperature dependence of electrical conductivity. In a complementary study, Shuai *et al.*[39] showed that Nb co-doping effectively suppresses ionized-impurity scattering and improves dielectric screening, thereby enhancing carrier mobility once the grain-boundary barriers are partially neutralized. These studies provide modern experimental and theoretical support for the barrier-controlled transport mechanism originally proposed by Seto, confirming its continued relevance in describing charge conduction across grain boundaries in polycrystalline semiconductors.

Collectively, these findings demonstrate that thermionic emission across grain boundaries is a universal transport pathway in polycrystalline semiconductors, manifesting in diverse systems ranging from chalcogenides and oxides to halide perovskites. While activation energies and barrier heights vary widely, their magnitude is consistently governed by the density and chemistry of GB trap states as well as dopant concentration. Importantly, recent evidence shows that halogen and alkali passivation (CdCl$_2$, Cl, Cu),[59–62] dopant redistribution,[50,51] and compositional tuning[56–58] can lower or eliminate deep states, thereby reducing barrier heights and enabling enhanced carrier collection. This convergence of bulk transport measurements, nanoscale imaging, and first-principles calculations consolidates Seto's classical model into a broader, chemistry-aware framework, underscoring that GB barriers are not fixed structural defects but chemically tunable electrostatic interfaces that can be deliberately engineered for improved device performance.[4,22,49–53,56–62]

3.2 Thermionic field emission and tunneling

3.2.1 Theoretical background. Thermionic field emission (TFE) represents an intermediate charge transport regime in which both thermal excitation and quantum tunneling contribute to carrier transmission across potential barriers at grain boundaries (GBs). Unlike pure thermionic emission (TE), which dominates at high temperatures, or Fowler–Nordheim-type field emission (FE), which becomes prominent at high electric fields and low temperatures, TFE operates when the barrier is sufficiently thin for partial tunneling yet retains a non-negligible thermal activation component. This interplay is particularly significant in polycrystalline semiconductors, where GB depletion widths are modulated by doping, interface states, and applied electric field.

The classical Fowler–Nordheim (FN) equation, derived under the assumption of triangular potential barriers and
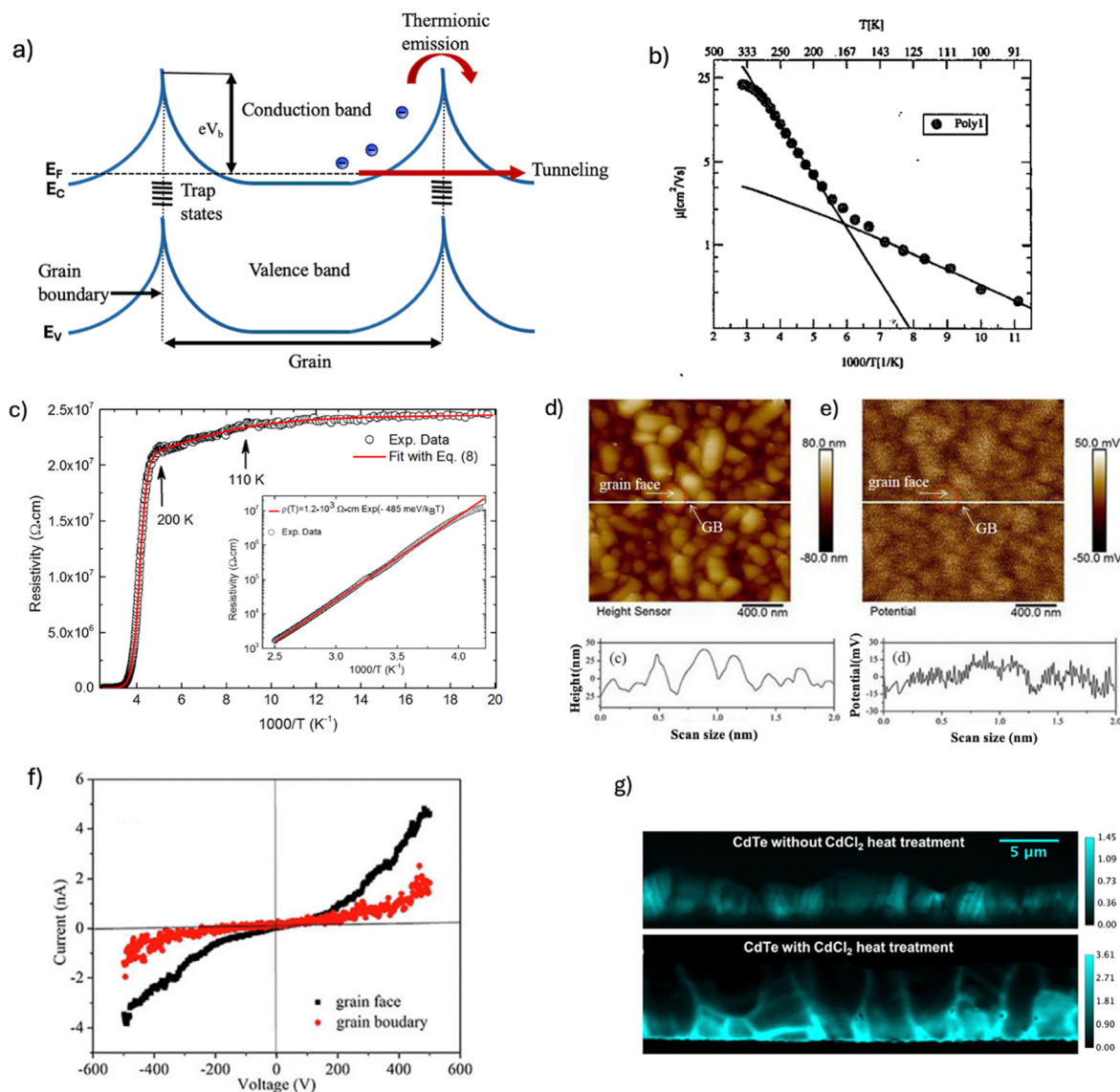
23682 | *J. Mater. Chem. C*, 2025, **13**, 23675–23695

This journal is © The Royal Society of Chemistry 2025

Fig. 3 (a) Schematic energy band diagram illustrating that thermionic emission occurs as carriers overcome grain boundary (GB) potential barriers formed by trap states (N_t), with possible tunneling contribution under strong fields. (b) Arrhenius plot of Hall mobility in polycrystalline $CuGaSe_2$ thin films, showing three temperature-dependent transport regimes: (I) high-temperature bulk-limited conduction, (II) intermediate-temperature thermionic emission over GB barriers (150 K–300 K), and (III) low-temperature hopping between localized states. Adapted (b) with permission from S. Schuler, "Charge carrier transport in polycrystalline $CuGaSe_2$ thin films," IEEE Proceedings, 2002. © 2002 IEEE.[27] (c) Temperature-dependent resistivity in Sb_2Se_3 fitted with a thermionic emission model in region II (200 K–110 K), yielding a GB barrier height of ~391 meV and a trap density of 3.4×10^{11} cm^{-2}; flattening at low temperature ($T < 110$ K) indicates transition to hopping-assisted transport (region III). Adapted with permission from N. Cifuentes *et al.*, *J. Phys. Chem. C*, 2020, **124** (14), 7677–7682. Copyright 2020 American Chemical Society.[54] (d) AFM topography and (e) KPFM surface potential image of NiO film highlighting nanoscale potential dips at grain boundaries, indicating the presence of electrostatic barriers, (f) local *I–V* curves measured by C-AFM across grain face and grain boundary regions in NiO show suppressed current at GBs, consistent with thermionic-limited transport under moderate bias. (d)–(f) are adapted from Yidong Zhang *et al.*, *Phys. E*, 2019, **111**, 75–78, with permission from Elsevier.[56] (g) EBIC images of CdTe before and after $CdCl_2$ treatment reveal enhanced carrier collection along GBs post-passivation, attributed to barrier height reduction and improved thermionic emission across GBs. Adapted with permission from Chen Li *et al.*, *Phys. Rev. Lett.*, 2014, **112**, 156103. © 2014 American Physical Society.[59]

zero-temperature tunneling, is widely used to describe FE:

$$J = \frac{q^3 E^2}{8\pi h \phi_B} e^{\left(-\frac{8\pi\sqrt{2m\phi_B^3}}{3qhE}\right)} \qquad (13)$$

where J is the current density, q the electron charge, E the electric field, h Planck's constant, m the electron mass, and ϕ_B the barrier height. However, this model fails to account for the finite-temperature effects and variations in barrier shape common in real materials. Murphy and Good extended this framework by incorporating image-force rounding and finite-temperature corrections, yielding an expression that predicts an "almost exactly" linear plot in the so-called Murphy–Good (MG) coordinates, thereby allowing more accurate extraction of

This journal is © The Royal Society of Chemistry 2025

J. Mater. Chem. C, 2025, **13**, 23675–23695 | **23683**

field emission parameters from experimental data.[52,64] Analytically, the tunneling probability $T(E)$ through a spatially varying potential $V(x)$ is commonly estimated using the Wentzel–Kramers–Brillouin (WKB) approximation:

$$T(E) \approx e^{\left(-\frac{2}{\hbar}\int_{x_1}^{x_2}\sqrt{2m(V(x)-E)}\,dx\right)} \quad (14)$$

where x_1 and x_2 are classical turning points. The exponential dependence on both electric field and barrier height renders this formalism highly sensitive to GB inhomogeneity, doping, and interface chemistry. Recent models have also introduced correction factors for barrier-lowering effects due to image charges, patch fields, and quantum confinement.[64–66]

The transition from TE to TFE and ultimately to FE is not abrupt but governed by a characteristic electric field ET, which depends on temperature, effective mass, barrier width, and doping level. Li et al. demonstrated this transition in β-Ga$_2$O$_3$ Schottky diodes, identifying a universal field ET that demarcates the regime boundaries.[67] Lin et al. further proposed a transport phase map that predicts the dominant conduction regime based on applied field and temperature, applicable to a wide range of semiconducting systems.[68]

3.1.2 Microscopic and experimental evidence of thermionic field emission. Extensive experimental studies across various polycrystalline materials corroborate the theoretical underpinnings of TFE transport. In degenerately doped ZnO:Al films, Nguyen et al. employed an Airy Function Transfer Matrix Method to quantify tunneling through GBs, revealing that at carrier concentrations exceeding 10^{19} cm^{-3}, GB depletion widths become narrow enough for tunneling to dominate.[69] Hüpkes et al. validated this behavior through mobility measurements, showing temperature-independent transport consistent with TFE, which could not be explained by TE or drift-limited models alone.[36]

In polycrystalline silicon, Sharma and Joshi constructed a comprehensive conduction model incorporating TE, TFE, and FE, demonstrating that resistivity and Hall mobility data could only be fitted when field-assisted tunneling components were included. Their findings highlighted the increasing dominance of TFE at low temperatures and high doping concentrations, particularly in S–GB–S (semiconductor–grain boundary–semiconductor) structures with narrow potential barriers.[70]

Lead chalcogenide systems such as PbSe exhibit similar behavior. Oxygen-sensitized polycrystalline PbSe films, widely used in infrared photodetectors, display nearly temperature-independent dark conductivity below 150 K—a signature of tunneling or hopping conduction through thin GB barriers.[71] These findings are consistent with the formation of inversion layers and narrow depletion regions under high electric fields, reducing the need for thermal activation. Emerging material platforms, such as hybrid halide perovskites and quantum-dot-perovskite composites, also demonstrate field emission under applied bias. In these systems, strong local fields induce carrier extraction via tunneling mechanisms, as observed through ultrafast transient absorption and photocurrent measurements.[72]

Microscopic techniques such as conductive atomic force microscopy (C-AFM) and Kelvin probe force microscopy (KPFM) have further illuminated the localized nature of GB barriers and field-enhanced tunneling. Zhang et al. used C-AFM and KPFM to investigate NiO thin films, observing non-linear I–V characteristics and suppressed surface potential (~ 17 meV) across ~ 60 nm-wide depletion regions at GBs—indicative of field-enhanced conduction channels.[56] In monolayer WSe$_2$, Su et al. employed tip-enhanced KPFM and photoluminescence imaging to reveal steep potential gradients and mid-gap states at tilted GBs, consistent with band bending and charge trapping that facilitate tunneling under high local fields.[73]

In CVD-grown polycrystalline graphene, Park et al. applied multi-probe scanning tunneling potentiometry (STP) to show that GBs act as high-resistance junctions, exhibiting localized voltage drops and reduced transmission probabilities. Although Dirac fermion transport introduces complexities, the observed conductance suppression across disordered GBs is consistent with tunneling-like behavior.[33] Finally, Chen et al. developed a spatially resolved polycrystalline cathode emission model incorporating grain orientation, local field enhancement, and barrier inhomogeneity, achieving excellent agreement with emission current maps observed experimentally via EBIC and cathodoluminescence.[65]

Collectively, these results establish that thermionic-field emission and tunneling are universal transport pathways in polycrystalline semiconductors once depletion widths are narrowed by high doping, field-induced band bending, or boundary defect chemistry. Across oxides, chalcogenides, hybrid perovskites, and even 2D materials, a common theme emerges: the transition from thermionic emission to field-assisted tunneling is governed less by temperature alone and more by the electrostatic and chemical environment of grain boundaries. Chemical dopant redistribution in ZnO:Al and poly-Si narrows depletion widths and enables tunnelling;[36,69,70] oxygen sensitization in PbSe modifies inversion layers and depletion regions;[71] and halide perovskites exhibit field-assisted extraction that is strongly dependent on GB defect passivation and local field gradients.[72] Microscopy studies further confirm that barrier inhomogeneity, mid-gap states, and electrostatic dips at GBs act as tunneling hot-spots.[56,73] Together, these findings refine the classical models of TE and FE into a chemistry-aware tunneling framework, underscoring that GB-mediated transport can be deliberately tuned through doping, compositional control, and targeted passivation to optimize devices ranging from transparent conductors to infrared photodetectors and thin-film photovoltaics.[33,36,56,65,67–73]

3.3 Hopping conduction

3.3.1 Theoretical background. In polycrystalline semiconductors characterized by strong disorder, small grain sizes, and elevated trap densities, charge carriers may become localized and unable to conduct via extended band states. Under these conditions—particularly at low temperatures—charge transport proceeds via thermally assisted tunneling between localized states, a mechanism known as hopping conduction. The

23684 | J. Mater. Chem. C, 2025, 13, 23675–23695

This journal is © The Royal Society of Chemistry 2025

foundational framework describing this phenomenon is Mott's Variable Range Hopping (VRH) model, which predicts the temperature dependence of conductivity in disordered systems as:

$$\sigma(T) = \sigma_0 \cdot e^{\left[-\left(\frac{T_0}{T}\right)^{1/4}\right]} \qquad (15)$$

where σ_0 is a prefactor and T_0 is a characteristic temperature dependent on the density of localized states near the Fermi level and the localization length—the spatial extent of carrier wavefunctions.[74] When long-range Coulomb interactions are non-negligible, they lead to a suppression of low-energy hopping states near the Fermi level, forming a soft Coulomb gap. In such cases, the Efros–Shklovskii VRH (ES-VRH) model becomes applicable, modifying the temperature dependence to:

$$\sigma(T) = \sigma_0 \cdot e^{\left[-\left(\frac{T_1}{T}\right)^{1/2}\right]} \qquad (16)$$

This stronger temperature dependence reflects enhanced localization due to repulsive interactions among hopping carriers.[75]

3.3.2 Microscopic and experimental evidence of hopping conduction.
Hopping conduction has been extensively validated in various disordered systems, particularly at cryogenic temperatures. In nanocrystalline CdSe, temperature-dependent conductivity measurements follow the Mott VRH model, indicating a high density of localized trap states and limited grain connectivity.[76]

In polycrystalline Sb_2Se_3, Cifuentes et al. observed a transition from thermionic emission to hopping conduction with decreasing temperature: between 160–250 K, an activation energy of $\sim$0.111 eV suggests defect-assisted transport, while below 110 K, the system obeys VRH behavior with $T_0 \approx 2.31 \times 10^6$ K (Fig. 3c).[54] Similar behavior is seen in $ZnSnO_3$ thin films, where VRH dominates below 100 K. The extracted density of states ($\sim10^{19}$ eV^{-1} cm^{-3}) corroborates this hopping framework.[77]

In oxidized nanocrystalline PbTe(In), hopping conduction prevails below 150 K, attributed to enhanced carrier localization along inversion channels at oxidized grain surfaces. Impedance spectroscopy confirmed a shift in transport dynamics, highlighting the role of microstructural evolution on conduction pathways.[78]

In Al-doped ZnO, VRH behavior is reported for underdoped films with weakly connected grains between 100–180 K.[79] Likewise, polycrystalline CdS and $CuInSe_2$ exhibit low-temperature hopping conduction across grain boundaries, often governed by trap-controlled transport.[80,81] In amorphous oxides such as IGZO, the stronger temperature dependence observed ($\propto T^{-1/2}$) below 150 K confirms ES-VRH behavior, suggesting a significant Coulomb gap due to electron–electron interactions in disordered networks.[82]

Experimental nanoscale techniques such as KPFM and C-AFM have provided direct visualization of these hopping pathways. For example, in NiO thin films, Zhang et al. observed localized current channels aligning with GB potential minima,

consistent with the formation of hopping percolation networks.[56] Similarly, in AZO films, KPFM studies confirm suppressed conductivity and potential barriers aligned with grain boundaries.[79]

Hopping conduction dominates at temperatures below $\sim$150–200 K, where thermal energy is insufficient to overcome grain boundary barriers or activate band-like transport. Instead, carriers tunnel between localized states within grains or across GBs. This behavior is exacerbated in materials with small grains, high trap densities, or oxygen/vacancy-related defects.[54,79,81] Collectively, these studies confirm that hopping conduction is a universal transport regime in disordered or defect-rich polycrystalline semiconductors, emerging whenever band-like or thermionic transport is suppressed by carrier localization. Across systems ranging from Sb_2Se_3 and CdSe to ZnO, PbTe, and IGZO, a consistent picture emerges: hopping behavior reflects the density and distribution of localized states at or near grain boundaries, which in turn are dictated by the underlying defect chemistry. Oxygen incorporation, vacancy complexes, and dopant under-saturation enhance localization and promote variable-range hopping.[54,56,75–82] Microscopy evidence further corroborates that GBs act as preferential sites for hopping pathways, with potential minima forming percolation networks that constrain long-range transport.[56,79] Thus, hopping conduction highlights the dual role of grain boundaries—not merely as scattering centers, but as chemically activated networks of localized states. Recognizing this chemical origin underscores that reducing trap density through boundary passivation, oxygen control, or dopant optimization remains central to suppressing hopping and restoring extended-state conduction in polycrystalline semiconductors (Table 1).

3.4 Conduction through threading crystallites

As discussed earlier, long-range charge transport is typically hindered in polycrystalline semiconductors by potential barriers at grain boundaries, localized trap states, and disorder-induced carrier scattering. However, in materials exhibiting columnar or interconnected microcrystalline morphologies, threading crystallites—elongated grains or grain cores aligned preferentially along the field direction—can serve as high-mobility conduction pathways. These microstructures resemble the ''shish–kebab'' morphology known from polymer crystallization, where a central thread (shish) aligns embedded crystallites (kebabs) directionally. Analogously, in semiconductor thin films, shish–kebab-like pathways offer percolative transport channels that effectively bypass high-resistance grain boundary regions.

3.4.1 Structural origin and morphological features.
Threading crystallites arise from anisotropic growth and recrystallization mechanisms, especially under post-deposition annealing, sensitization, or templated nucleation. In lead salt systems such as PbSe/CdSe nanocrystalline heterostructures, cross-sectional SEM and XRD data reveal elongated PbSe cores aligned vertically through the film, with CdSe forming reconfigurable shells around them.[84] During oxygen or iodine-based

This journal is © The Royal Society of Chemistry 2025

J. Mater. Chem. C, 2025, **13**, 23675–23695 | **23685**

Table 1 Summary of conduction mechanisms in polycrystalline semiconductors

Mechanism	Physical origin	Governing equation/model	Dominant conditions	Representative materials
Drift–diffusion[4,22–26,28]	Carrier motion under electric field (drift) and concentration gradient (diffusion); GBs add barriers and scattering	$J = qn\mu E + qD\dfrac{dx}{dn}$	$E < 10^3$ V cm^{-1}; moderate T (200–400 K); carriers not strongly depleted at GBs	Si, CIGS, TFT
Thermionic emission[4,27,50,54–57,59,61]	Thermal excitation of carriers over GB potential barriers	$J = A \times T^2 e^{\frac{-q\varphi_B}{KT}}$	High T (>200 K); moderate doping (10^{14}–10^{16} cm^{-3}). Barrier heights 60–400 meV; reduced after halogen/alkali passivation	CuGaSe$_2$, Sb$_2$Se$_3$, ZnO, CdTe, PbS, NiO, MAPbI$_3$
Thermionic field emission (TFE) & tunneling[33,36,56,65,67–70,73]	Mixed thermal activation + tunneling through narrow GB barriers at high doping/field	$J = \dfrac{q^3 E^2}{8\pi h\phi_B} e^{\left(-\frac{8\pi\sqrt{2m\phi_B^3}}{3qhE}\right)}$	High doping ($>10^{17}$ cm^{-3}) thin barriers (<5 nm); temperature-independent conduction at high doping; tunneling-dominated transport	ZnO:Al, poly-Si, PbSe, NiO, perovskites, WSe$_2$, graphene
Hopping conduction[54,56,74–82]	Localized carriers hop between defect states at GBs or within grains	$\sigma(T) = \sigma_0 \cdot e^{\left[-\left(\frac{T_0}{T}\right)^{1/4}\right]}$ (VRH)	Dominant <150–200 K; Low T (<150 K); high density of localized states; disordered GBs	Sb$_2$Se$_3$, CdSe, ZnSnO$_3$, PbTe, AZO, CdS, CuInSe$_2$, IGZO, NiO
Threading crystallites[83–85]	Columnar/elongated grains aligned with field; core–shell structures enable anisotropic conduction	Percolative current along oriented crystallites	Highly textured polycrystals; conductive threads	PbSe/CdSe core–shell, sensitized PbSe, 1D PbSe arrays

Table 2 Grain boundary engineering strategies and their impact on carrier transport

Strategy	Description	Impact on carrier transport	Representative materials
Chemical passivation (Cl, Cu, alkali metals, H)[6,59,61,86,87]	Incorporation of passivating agents (e.g., Cl, Cu, H) at GBs to neutralize/compensate trap states via bond formation/charge reduction	Reduces recombination, lowers barrier height, enhances mobility and lifetime	CdTe, CIGS, Si
GB potential barrier tuning (dopant/trap control)[4,50,57]	Modulate GB electrostatics by adjusting dopant density and filled trap density	Tailors barrier height and band bending; balances conductivity vs. recombination	Perovskites
Grain orientation control/texturing[88–90]	Promote highly oriented/columnar grains to reduce effective GB density and align internal fields.	Enhances carrier collection along preferred paths (GB-enhanced EBIC after CdCl$_2$).	Sb$_2$Se$_3$, Cu$_2$O, ZnO:Al
GB passivation by oxidation/secondary phase segregation[6,55,84]	Controlled O$_2$/air or halogen (Cl/I) treatments modify GB chemistry and band alignment.	Suppresses active traps, may form conductive channels	PbS/PbSe
Ion migration suppression[57,58]	Engineer GBs (dopants/additives, passivation) to limit halide/ion transport pathways.	Enhances stability, reduces hysteresis, preserves carrier lifetimes by limiting bias-induced contact potential difference (CPD) changes at GBs.	Halide perovskites
Nanocrystallite/GB size optimization[27,54]	Controlling grain size via annealing or deposition conditions	Balances scattering vs. barrier effects; larger grains reduce GB density	Sb$_2$Se$_3$, CuGaSe$_2$
Grain-boundary metallization and anti-barrier interface engineering[17,91]	Introduction of metallic inclusions (Nb, Ta) and low-work-function interlayers (W, Mo) at GBs to form metal–semiconductor interfaces that reduce or invert potential barriers.	Enhances carrier mobility and electrical conductivity without degrading Seebeck coefficient	n-type Mg$_3$(Sb,Bi)$_2$

sensitization, PbSe grains undergo ripening and axial elongation, creating conductive cores separated from surface oxides or depletion layers. A similar evolution is observed in charge separation junction (CSJ) models, where p-type PbSe cores are surrounded by n-type shells formed via halogen or oxygen doping. These structures can spontaneously interconnect across film depth, forming conductive threads between contacts.[83,85]

Such arrangements have also been observed in other systems, including vertically aligned 1D PbSe microcrystals grown via wet chemical methods or MBE, where grain boundaries are absent in the growth direction but present laterally, confirming preferential anisotropy.[85]

3.4.2 Transport mechanism and theoretical consideration. Charge carriers, particularly holes in p-type cores, traverse these crystalline threads with minimal scattering or barrier interaction. Simultaneously, photogenerated electrons are confined to the n-type or oxide-rich shell, achieving spatially separated dual-lane transport. This reduces recombination and allows photogenerated carriers to transit through aligned conductive channels without undergoing significant trapping.

The mechanism aligns with quasi-1D percolation theory and dual-path transport models where carrier mobility is not averaged over a randomly oriented grain network but is instead defined by the presence and continuity of these aligned threads. In CSJ simulations, recombination is minimized due

23686 | J. Mater. Chem. C, 2025, **13**, 23675–23695

This journal is © The Royal Society of Chemistry 2025

to this structural segregation, yielding enhanced lifetime and detector responsivity that scale with crystallite core continuity and shell integrity.[83] Mathematically, the recombination rate reduction in this model is expressed as:

$$R_{\text{total}} = r_{\text{rad}}np + r_{\text{Aug-e}}n^2p + r_{\text{Aug-h}}np^2 + \frac{N_{\text{rec}}}{\tau_{\text{SRH-e}}} + \frac{p_{\text{rec}}}{\tau_{\text{SRH-p}}} \quad (17)$$

Lowering n or p due to spatial separation significantly reduces R_{total}, improving effective carrier lifetime τ, and thus signal gain.

3.4.3 Experimental evidence. Recent experiments on PbSe/CdSe photoconductive films grown by vapor phase deposition (VPD) have revealed that annealing in oxygen reshapes CdSe shells and promotes PbSe core elongation, forming interconnected "threading" grain cores (Fig. 4).[84]

Further, the "charge separation" model proposed by Zhao *et al.* simulates and explains how these threading cores form continuous carrier lanes for majority carriers, enabling transport across multiple grains without cross-type recombination.[83] Their numerical simulations showed $>40\times$ enhancement in carrier lifetime and $>45\times$ increase in responsivity due to this structure. Additionally, microstructural analysis of MBE-grown or chemically grown 1D PbSe arrays confirms that shish–kebab structures form naturally on (100)-oriented facets and exhibit superior photoluminescence and *I–V* behavior compared to conventional polycrystalline films.[85]

Taken together, these studies establish that conduction through threading crystallites represents a morphology-driven transport pathway that fundamentally differs from conventional grain-boundary-limited conduction. While demonstrated most clearly in PbSe/CdSe heterostructures, the principle is general: axially aligned grains or core–shell structures create quasi-1D channels that bypass lateral grain boundary barriers and provide spatial separation of electrons and holes.[83–85] This dual-lane conduction suppresses recombination and enhances mobility, explaining high responsivity and long carrier lifetimes in sensitized PbSe detectors and related films. Importantly, the formation of these threaded cores is not purely structural but is strongly influenced by chemical treatments such as oxygen or halogen sensitization, which drive inversion layers and core elongation.[83,84] Thus, the shish–kebab mechanism highlights a critical interplay between microstructural anisotropy and grain boundary chemistry, underscoring that device performance can be optimized not only by reducing defect density but also by programming grain connectivity and orientation. This morphology-based conduction model broadens the design space for polycrystalline semiconductors, offering a scalable alternative to single-crystal growth for optoelectronic and detector applications.[83–85]

4 Factors affecting carrier transport

Carrier transport in polycrystalline semiconductors is intricately influenced by both structural and electrical heterogeneities. In contrast to single crystals, the presence of grain boundaries (GBs), microstructural defects, and spatially non-uniform dopant distributions introduces localized variations in electrostatic potential, scattering rates, and recombination dynamics. This section systematically explores the major physical, structural, and material-dependent factors that modulate charge carrier conduction in polycrystalline films.

4.1 Microstructural features

4.1.1 Grain size and morphology. Grain size is a dominant parameter in defining the extent of grain boundary scattering and barrier-limited transport. As grain size decreases, the number of grain boundaries per unit length increases, which in turn amplifies potential barriers and trap densities that
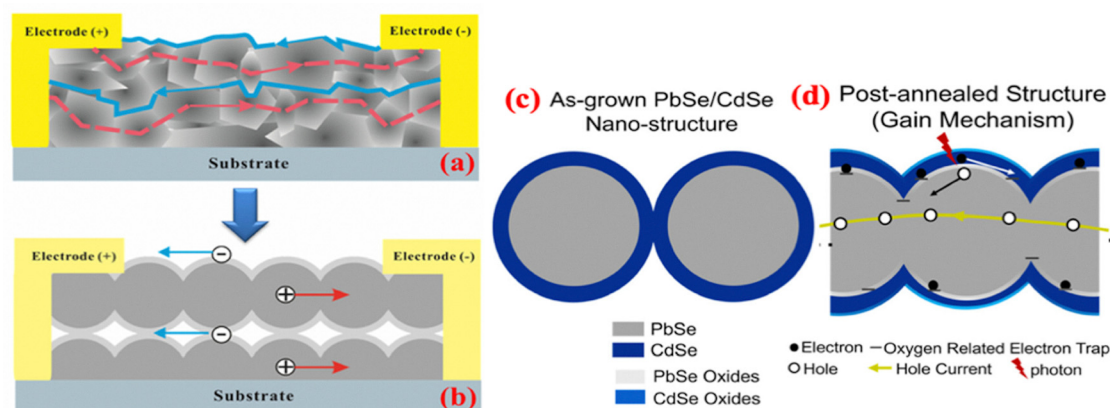

Fig. 4 Conceptual and simulated representations of the charge separation and threading crystallite transport model in sensitized polycrystalline PbSe films. (a) Schematic of p-type to n-type inversion of the surface of crystallites induced by oxygen sensitization, forming a core−shell structure. (b) Idealized polycrystalline geometry used in the numerical model, where each sphere represents an individual crystallite and its corresponding grain boundary environment. (a) and (b) are adapted from B. Weng *et al.*, *Proc. SPIE*, 2013, **8993**, 8993−37, with permission from SPIE.[85] (c) Pristine core−shell morphology showing spatial separation of electrons and holes across the PbSe/CdSe interface. (d) Optimized structure exhibiting vertically aligned (threaded) PbSe cores, enabling long-range hole transport, injection of new carriers, and recombination suppression by confining minority electrons to the shell. (c) and (d) are adapted from R. M. Mirzaei and Z. Shi, *Appl. Phys. Lett.*, 2024, **125** (8), with the permission of AIP Publishing.[84]
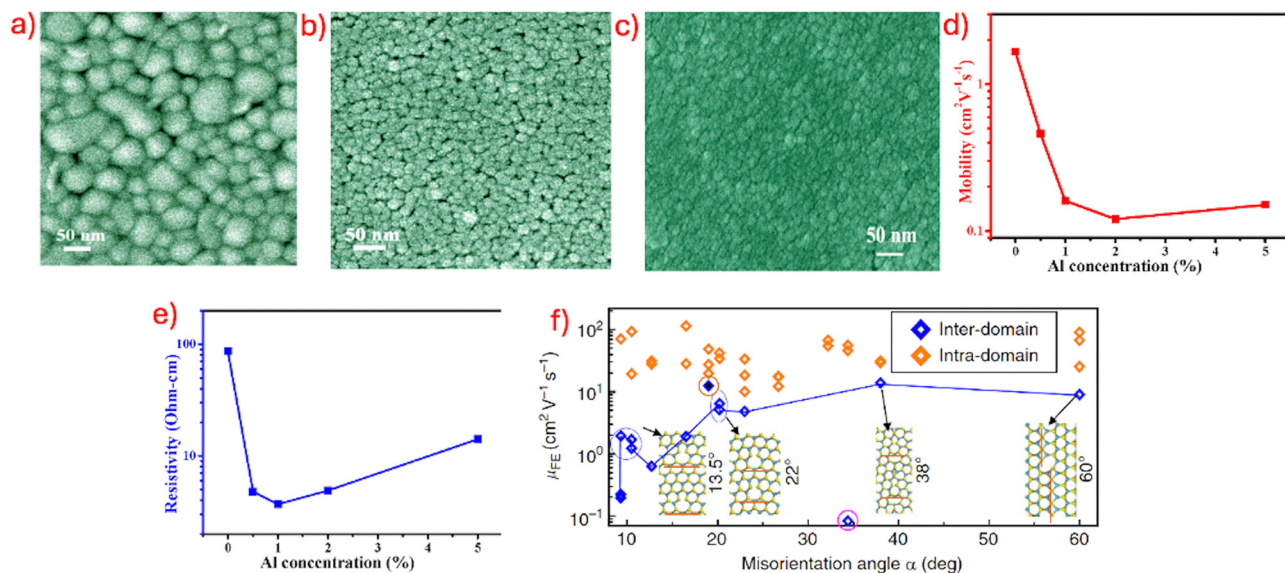
This journal is © The Royal Society of Chemistry 2025

J. Mater. Chem. C, 2025, **13**, 23675–23695 | **23687**

Fig. 5 Impact of grain boundary structure and doping on carrier transport in polycrystalline semiconductors. (a)–(c) FESEM images showing grain size refinement in ZnO with increasing Al doping from 0% to 5%, resulting in denser grain boundaries. (d)–(e) Hall effect measurements reveal a monotonic decrease in mobility and an increase in resistivity with increasing Al content, attributed to enhanced grain boundary scattering. (f) Mobility variation as a function of misorientation angle α, indicating increased barrier-limited transport across high-angle grain boundaries ($\alpha > 20°$), where mobility saturates below 16 cm^2 V^{-1} s^{-1}. Adapted (a)–(e) from B. Mahapatra and S. Sarkar, *Heliyon*, 2022, **8** (10), e10961, with permission from Elsevier,[79] and Adapted (f) from T. H. Ly, D. J. Perello, J. Zhao, *et al.*, *Nat. Commun.*, 2016, **7**, 10426. Licensed under CC BY 4.0 (**https://creativecommons.org/licenses/by/4.0/**).[93]

carriers must overcome. For example, studies have shown that larger grains in CdTe films correlate with enhanced carrier lifetimes and improved device performance. For instance, CdTe films with grain sizes exceeding 1 μm exhibit longer carrier diffusion lengths, leading to higher photovoltaic efficiencies.[10] In Al-doped ZnO (AZO) films, increasing the Al concentration leads to a reduction in grain size. This grain refinement results in a higher density of GBs, which can introduce potential barriers and trap states, adversely affecting carrier mobility. Mahapatra and Sarkar systematically demonstrated that increasing Al doping leads to pronounced grain refinement—from an initial broad distribution of 17–115 nm in undoped ZnO to a uniform size range of ∼20–25 nm at 1% Al. This grain size reduction results in a higher density of grain boundaries, which introduce potential barriers and localized trap states. Hall measurements confirmed that the electrical mobility decreased markedly with increasing dopant concentration, a trend attributed to enhanced grain boundary scattering and interruption of conduction paths (Fig. 5(a)–(e)). These observations underscore the direct correlation between grain-scale structural changes and charge transport limitations in AZO polycrystalline films.[79]

The relationship between grain size and mobility is often captured through thermionic emission models, where mobility μ follows an Arrhenius-type dependence on temperature and barrier height Φ_B. Larger grains reduce the number of GBs encountered per unit length, effectively minimizing the impact of such barriers on carrier transport. These findings underscore that grain size is not merely a structural parameter but a key determinant of trap density and electrostatic barrier distribution, where chemical dopants and processing conditions jointly

govern the balance between refinement-induced scattering and enhanced carrier collection.[10,79]

4.1.2 Grain orientation and crystallinity. The orientation of grains and the degree of crystallographic alignment can facilitate or impede charge transport. Anisotropic materials such as Sb$_2$Se$_3$ exhibit chain-like [001] crystal orientations, where carriers move more efficiently along the one-dimensional van der Waals chains. Sb$_2$Se$_3$ possesses a quasi-one-dimensional crystal structure, where charge transport is more efficient along the [001] direction. Films with grains oriented along this direction demonstrate enhanced carrier mobility and reduced recombination losses. Controlling the growth conditions to favor this orientation is crucial for optimizing device performance.[88] This effect is attributed to the reduced number of misoriented grain boundaries and the quasi-one-dimensional nature of carrier conduction pathways.

High crystallinity is also essential for minimizing intra-grain scattering.[95] Polycrystalline films synthesized *via* low-temperature methods (*e.g.*, sol–gel or spin coating) often suffer from nanocrystallinity and poor lattice ordering, resulting in higher scattering and defect densities.[96,97] Conversely, high-temperature vapor deposition methods yield larger and more ordered grains, which enhance carrier mobility.[97] Thus, grain orientation and crystallinity dictate whether GBs behave as high-barrier interfaces or quasi-one-dimensional conduction pathways, emphasizing that chemical control of growth kinetics and thermal treatments is as critical as structural alignment for optimizing transport.[88,95–97]

4.1.3 Grain boundary type: low angle *vs.* high angle *vs.* twin. Grain-boundary misorientation critically influences charge transport in polycrystalline materials. Low-angle grain

23688 | *J. Mater. Chem. C*, 2025, **13**, 23675–23695

This journal is © The Royal Society of Chemistry 2025

boundaries (LAGBs), defined by misorientation angles <10–$15°$, consist of regular dislocation arrays and introduce minimal band bending or trap states. In contrast, high-angle grain boundaries (HAGBs) contain amorphous dislocation networks and deep defect states that foster significant space-charge depletion and Fermi-level pinning, impeding carrier flow. In a study on 2D MoS_2, Ly et al. demonstrated a non-linear increase in interdomain mobility with misorientation angle—from near zero below $9°$ to saturation around $20°$—confirming that LAGBs act as weak, low-barrier conduits, while HAGBs induce pronounced barriers to conduction (Fig. 5f).[93] Similar effects are observed in metals; Bishara et al. showed that thin-film Cu bicrystals exhibit approximately double the resistivity at LAGBs (~14–$18°$) versus HAGBs, due to increased dislocation density and associated strain fields.[98]

Twin boundaries are a unique class of planar defects characterized by a mirror symmetry. They typically introduce minimal disruption to the lattice potential and are often electrically benign or even beneficial. In CdTe and Sb_2Se_3, twin boundaries have been shown to act as low-resistance pathways for carrier flow. TEM studies have confirmed that twin boundaries do not introduce significant mid-gap states, in contrast to general high-angle GBs.[21,99] Taken together, these observations highlight that GB type governs carrier transport far beyond geometry, with high-angle GBs acting as recombination-active traps, while coherent twin boundaries remain chemically and electronically benign, offering low-resistance channels for transport.[21,93,98,99]

4.2 Electrical effects at the grain boundaries

4.2.1 Band bending and depletion regions. Grain boundaries often accumulate charge due to the presence of defect states, which leads to the formation of space charge regions or depletion zones on either side of the boundary. This results in band bending that creates electrostatic barriers for carriers. Seto's model provides an analytical expression for the GB barrier height Φ_B.[4]

In NiO thin films, KPFM measurements have demonstrated that GBs exhibit significant potential variations compared to grain interiors. These variations are linked to differences in work function and electronic conductivity, suggesting that GBs in NiO can act as barriers to charge transport.[56] Consequently, GB band bending emerges as a chemically tunable parameter: defect passivation, doping, or compositional engineering can reshape depletion profiles and barrier heights, turning recombination-active boundaries into quasi-transparent interfaces.[4,56]

4.2.2 Trap states and defect density. Trap states at GBs can either be shallow or deep, with the latter severely limiting carrier lifetimes and enhancing non-radiative recombination. Techniques like deep-level transient spectroscopy (DLTS) and time-resolved photoluminescence (TRPL) have been employed to probe the nature of these defects.[94,100]

In CdTe thin-film solar cells, chlorine (Cl) incorporation through post-deposition $CdCl_2$ treatment leads to the preferential segregation of Cl atoms at grain boundaries (GBs), where

they play a crucial role in modifying the local defect chemistry. Using advanced characterization techniques such as scanning transmission electron microscopy (STEM), energy-dispersive X-ray spectroscopy (EDX), and nanoscale secondary ion mass spectrometry (NanoSIMS), researchers have directly observed elevated Cl concentrations at GBs compared to grain interiors. This segregation alters the electronic environment of GBs, either passivating or modifying deep-level trap states that typically act as non-radiative recombination centers. While Cl can effectively passivate some defect sites, excessive or uneven Cl accumulation may lead to the formation of complex defect clusters that introduce new trap states. These defect-mediated recombination pathways can limit the collection of photogenerated carriers before they reach the junction, thereby reducing device efficiency. Experimental findings are supported by density functional theory (DFT) simulations, which show that Cl atoms can replace Te atoms or occupy interstitial sites at GBs, leading to a reduction in deep mid-gap states and suppression of Fermi level pinning.[101,102]

Overall, the impact of GB traps demonstrates that recombination is governed less by structural disorder alone and more by the local defect chemistry, where targeted passivation (e.g., Cl incorporation) can transform deep recombination centers into electronically benign sites.[94,100–102]

4.3 Material specific factors

4.3.1 Doping level and compensation:. Doping is a critical parameter that affects both carrier concentration and the width of depletion regions at GBs. As doping increases, the Debye length decreases, resulting in narrower depletion zones and enhanced thermionic or tunneling-based transport. However, excessively high doping can lead to enhanced ionized impurity scattering and reduced mobility.[4,36]

In SnO_2:F films, conductivity initially increases with fluorine doping as carrier concentration increases. However, Hall measurements show that beyond $\sim1.2 \times 10^{20}$ cm^{-3}, mobility peaks (~42 cm^2 V^{-1} s^{-1}) and then declines due to enhanced ionized impurity scattering.[103] These studies confirm that doping serves as a double-edged lever: while moderate levels shrink depletion widths and enhance transport, excessive doping induces Coulombic scattering, making compensation control and chemical homogeneity essential for mobility optimization.[4,36,103]

4.3.2 Passivation strategies. Grain boundary passivation involves chemically modifying grain boundaries to neutralize trap states or reduce electrostatic barriers that impede carrier transport. Several strategies have been developed for this purpose. Halide treatments, such as those using chlorine or bromine, are widely applied in CdTe and perovskite systems to saturate dangling bonds and suppress recombination. Alkali doping, particularly with elements like sodium (Na) and potassium (K), has proven effective in thin-film photovoltaics by introducing shallow donor states and modifying GB electronic properties. For instance, in $Cu(In,Ga)Se_2$ (CIGS) solar cells, post-deposition treatment with sodium fluoride (NaF) has been shown to directly passivate grain boundaries. Using nanoscale

This journal is © The Royal Society of Chemistry 2025

J. Mater. Chem. C, 2025, **13**, 23675–23695 | **23689**

optoelectronic characterization, Nicoara *et al.* demonstrated that Na incorporation reduces non-radiative recombination at GBs and improves junction quality, resulting in a significant enhancement of the open-circuit voltage and overall device efficiency.[6] Additionally, organic monolayers have been employed in oxide semiconductors to reduce surface states and stabilize potential profiles, further contributing to carrier lifetime improvements.[104,105] Moreover, Hydrogen passivation, first shown in polycrystalline silicon-remains widely used to neutralize grain-boundary dangling bonds *via* Si–H formation, reducing traps and barrier heights and continuing to serve as a key defect-control method in modern silicon photovoltaics.[86,87]

Collectively, these results show that passivation is not a one-size-fits-all remedy but a chemically specific intervention, where alkali fluorides, halides, hydrogen, or organic modifiers each alter trap energetics in distinct ways, reinforcing GB chemistry as the decisive factor in suppressing recombination and enhancing transport (Fig. 6(c–d)).[6,48,86,87,104,105]

4.3.3 Fabrication method and crystallinity. The method of film synthesis directly influences the resultant microstructure, defect landscape, and ultimately the electrical performance of polycrystalline materials. High-temperature vacuum-based techniques such as molecular beam epitaxy (MBE), chemical vapor deposition (CVD), and pulsed laser deposition (PLD) are known to produce thin films with larger, highly oriented grains and lower defect densities. These structural advantages translate into enhanced carrier mobilities and reduced leakage currents due to fewer grain boundaries and minimized trap-assisted recombination pathways.[106]

In contrast, solution-processed methods like the sol–gel technique often yield films with nanoscale grain sizes, higher porosity, and less uniform microstructure. These characteristics contribute to increased grain boundary scattering, higher trap densities, and reduced electrical conductivity. For example, sol–gel derived ZnO thin films have shown smaller grain sizes and poorer crystallinity at lower annealing temperatures, which corresponded to inferior electrical characteristics. However, controlled post-annealing at elevated temperatures can partially mitigate these issues by promoting grain coalescence and improving film densification.[107]

The difference in electrical performance between sol–gel and PLD-grown films is evident in studies on $ZnSnO_3$ thin films. While direct studies on $ZnSnO_3$ by Islam *et al.* could not be verified, similar investigations by Cai *et al.* demonstrated that Ta-doped $ZnSnO_3$ films fabricated *via* sol–gel methods exhibited limited conductivity and mobility, largely attributed to the presence of voids and microstructural inhomogeneity. These films often require high-temperature processing (>500 °C) to achieve crystallization and improved transport properties.[108]

Together, these findings highlight the importance of selecting and optimizing the film deposition technique for applications in photovoltaics, thermoelectrics, and sensors. By engineering the grain structure and minimizing defect-mediated transport barriers, significant improvements in carrier transport can be achieved.

5 Design guidelines and outlook

5.1 Design guidelines for optimizing carrier transport

Optimizing charge transport in polycrystalline semiconductors necessitates precise control over grain boundary (GB) structures, chemical compositions, and electronic properties. As GB-mediated mechanisms, such as thermionic emission, often dominate transport behavior, the following strategies are pivotal in mitigating transport barriers and enhancing carrier mobility.

5.1.1 Grain boundary passivation and control. Grain boundaries, often rich in charged trap states and structural disorders, introduce electrostatic barriers that impede carrier mobility. Effective passivation—through chemical treatments, controlled doping, or incorporation of passivating interlayers—can neutralize interface states, reduce barrier heights, and suppress recombination. For example, in $Cu(In,Ga)Se_2$ (CIGSe) solar cells, Nicoara *et al.* provided direct experimental evidence that post-deposition treatments using alkali fluorides (*e.g.*, KF, RbF, CsF) effectively passivate grain boundaries. Through nanoscale optoelectronic characterization, they showed that such treatments significantly reduce the density of charged defects at GBs, leading to enhanced open-circuit voltage and carrier collection efficiency.[6] These advances highlight the importance of grain boundary engineering in optimizing the performance of polycrystalline photovoltaic material.

5.1.2 Doping optimization and depletion width engineering. The barrier height at grain boundaries inversely correlates with free carrier concentration, as predicted by Seto's model.[4] Controlled doping can narrow depletion regions and suppress electrostatic barriers. However, excessive doping may lead to ionized impurity scattering or tunneling-mediated leakage. Optimizing doping profiles is crucial to balance carrier density enhancement with thermionic emission dominance.[109]

5.1.3 Crystallographic orientation and texturing. Preferred grain orientations—along high-mobility crystallographic axes like [100] in Cu_2O or (0001) *c*-axis in AZO—can reduce the prevalence of high-angle grain boundaries and associated scattering. For example, Cu_2O films sputtered with [100] texture exhibit greater lateral mobility post-annealing compared to [111]-textured films,[89] while ZnO:Al films with sharper *c*-axis alignment show reduced resistivity and enhanced carrier mobility due to decreased grain boundary scattering.[90] Engineering film texture through substrate choice or thermal treatments, thus effectively minimizes scattering interfaces and promotes in-plane carrier transport.

5.1.4 Twin boundary engineering. Unlike random grain boundaries, coherent twin boundaries (CTBs) possess mirror symmetry and low formation energy, resulting in minimal electronic disturbance and reduced recombination activity. In materials such as halide perovskites, ferroelastic twin boundaries have been shown to be electronically benign and do not hinder carrier transport or act as trap-rich recombination centers.[5] Similarly, in thermoelectric Bi_2Te_3, twin boundaries can influence carrier concentration and scattering, with studies showing that 60° twins may act as localized electron

23690 | *J. Mater. Chem. C*, 2025, **13**, 23675–23695

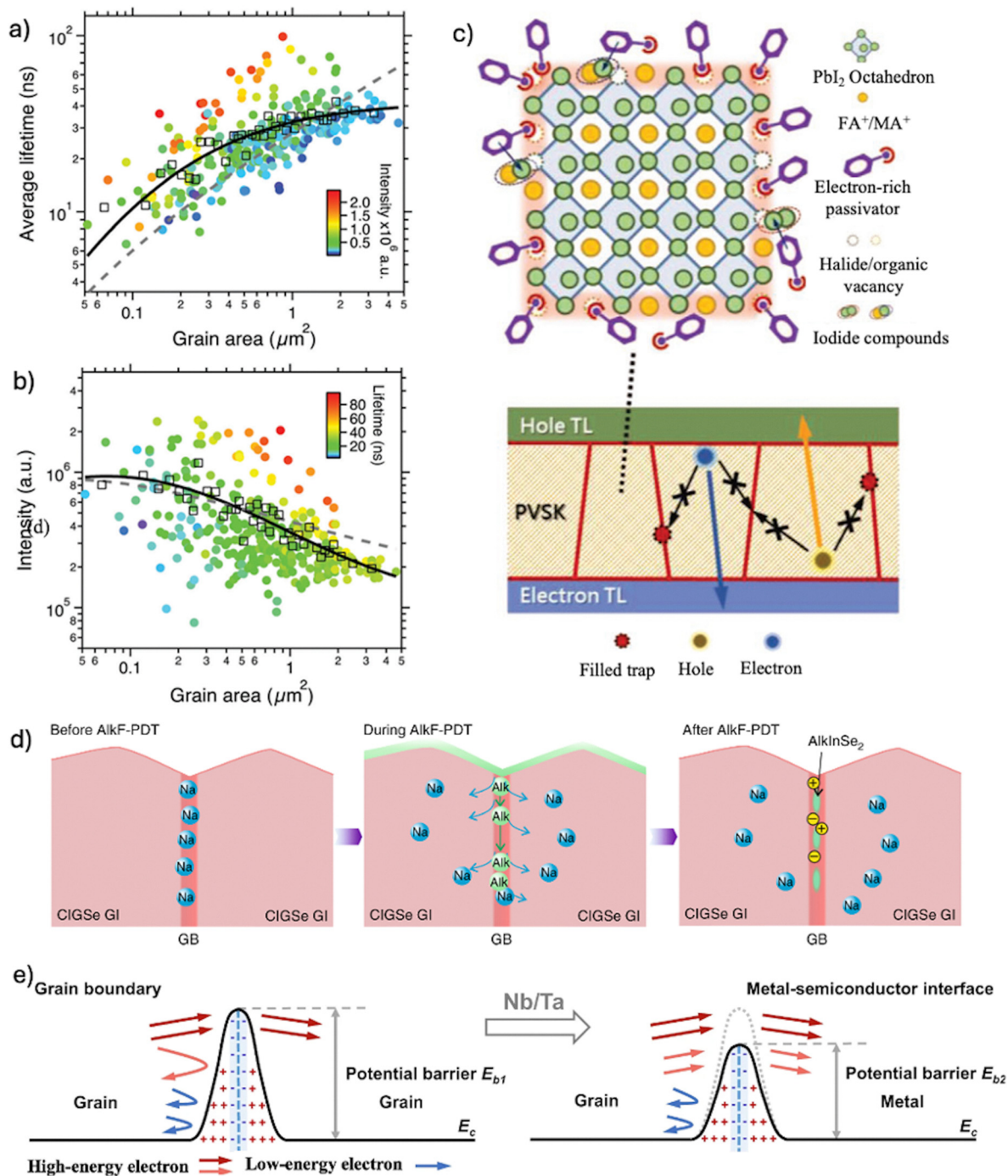This journal is © The Royal Society of Chemistry 2025

Fig. 6 The influence of grain size, trap states, and passivation strategies on carrier transport in polycrystalline semiconductors. (a) and (b) Fluorescence lifetime imaging microscopy (FLIM) analysis of ∼300 perovskite grains reveal that smaller grains exhibit shorter photoluminescence (PL) lifetimes and reduced intensity, indicating increased trap-assisted non-radiative recombination at GBs. (a) and (b) are adapted from Mengjin Yang *et al.*, *Phys. Chem. Chem. Phys.*, 2017, **19**, 5043–5050, with permission from the Royal Society of Chemistry.[94] (c) Schematic illustration of how electron-rich molecular passivators mitigate defect states (*e.g.*, halide vacancies) and suppress trap-assisted recombination by stabilizing interfacial electron clouds at the perovskite grain surfaces. Adapted from Qihuang Gong *et al.*, *Adv. Mater.*, 2020, **32** (39), 2005506. Licensed under CC BY 4.0 (**https://creativecommons.org/licenses/by/4.0/**).[48] (d) Post-deposition treatment (PDT) in CIGSe films enables passivating recombination-active sites and enhancing charge collection. Adapted from Nicoleta Nicoara, X. Fu, T. P. Weiss, *et al.*, *Nat. Commun.*, 2019, **10**, 3980. Licensed under CC BY 4.0 (**https://creativecommons.org/licenses/by/4.0/**).[6] (e) Schematic illustration showing the difference in interfacial potential barriers (E_b) at a conventional grain boundary and at a metal–semiconductor interface in n-type $Mg_3(Sb,Bi)_2$. The metal inclusion reduces the barrier height and promotes carrier transmission across the interface. Adapted from Li *et al.*, *Nat. Commun.*, 2023, **14**, 7428. Licensed under CC BY 4.0 (**https://creativecommons.org/licenses/by/4.0/**).[17]

This journal is © The Royal Society of Chemistry 2025

J. Mater. Chem. C, 2025, **13**, 23675–23695 | **23691**

sources.[82,110] Although direct methods for inducing extended twin networks remain underexplored, modifying deposition temperature or stress conditions during growth can influence twin density. Engineering CTBs thus holds promise for enhancing carrier mobility in polycrystalline semiconductors by offering low-defect conduction pathways.

5.1.5 Low-defect film deposition. Reducing bulk and interfacial defects during growth directly improves transport. Techniques such as low-pressure chemical vapor deposition (CVD) and laser crystallization have been employed to produce high-performance thin-film semiconductors with low defect densities.[111,112]

5.1.6 GB metallization/anti barrier engineering. Recent progress in n-type $Mg_3(Sb,Bi)_2$ thermoelectrics highlights how grain-boundary metallization and anti-barrier engineering can effectively overcome interfacial resistivity. Li et al.[17] demonstrated that incorporating Nb or Ta nano-inclusions at grain boundaries forms metal–semiconductor interfaces with reduced potential barriers, which facilitate carrier transmission and significantly enhance electrical conductivity and mobility (Fig. 6e). This approach yielded power factors exceeding 30 μW cm^{-1} K^{-2} and peak ZT values up to 2.04 at 798 K. Building upon this concept, Li et al.[91] employed low–work-function W and Mo interlayers to create so-called "anti-barrier" interfaces, where downward band bending produces electron-rich channels that virtually eliminate grain-boundary resistance. Together, these studies demonstrate that strategic interfacial band-structure engineering can transform conventional resistive grain boundaries into highly conductive pathways, offering a practical and scalable route to enhance carrier transport in polycrystalline thermoelectric materials.

In summary, optimizing charge transport in polycrystalline semiconductors requires coupling grain boundary chemistry with microstructural control. Passivation treatments, such as Cl in CdTe and perovskites,[101,102] or alkali fluorides in CIGSe,[6] neutralize traps and reduce recombination. Controlled doping narrows depletion widths without inducing excessive scattering, consistent with Seto's barrier model.[4,109] Orientation control in Cu_2O and ZnO,[89,90] and benign twin boundaries in perovskites,[5] and Bi_2Te_3,[110] provide low-resistance pathways. Moreover, low-defect growth methods such as CVD or laser crystallization further enhance mobility.[111,112] Finally, recent advances in n-type $Mg_3(Sb,Bi)_2$ further illustrate the principle, where grain-boundary metallization and anti-barrier interface engineering have effectively eliminated resistive barriers and yielded record thermoelectric performance.[17,91] Collectively, these strategies highlight that transport is dictated less by grain size alone than by the chemical and structural state of GBs, which can be deliberately engineered for high-performance photovoltaic, thermoelectric, and optoelectronic devices (Table 2).

5.2 Outlook for polycrystalline semiconductors

The continued advancement of polycrystalline semiconductors in optoelectronics, thermoelectrics, and sensors hinges on the ability to design grain architectures and control local transport mechanisms. Future progress will require close integration of materials chemistry, device physics, and data-driven design strategies.

5.2.1 Correlated imaging and transport analysis. A major limitation in current studies is the separation between structural imaging and transport characterization. Advanced correlative techniques that combine Kelvin probe force microscopy (KPFM) with electron beam-induced current (EBIC) or conductive AFM (C-AFM) have enabled direct visualization of potential barriers and charge transport at grain boundaries. Liu et al. demonstrated such an integrated approach in hybrid perovskites, revealing spatially resolved conduction bottlenecks associated with GB chemistry and band bending.[113]

5.2.2 Grain-by-grain transport statistics. Machine-learning-assisted microscopy and data-driven transport modeling are emerging as powerful tools to analyze grain-level variations. Zhang et al. showed that statistical analysis of barrier heights, mobility, and GB geometry across many grains enables predictive modeling of macroscopic transport, forming the basis for inverse materials design.[114]

5.2.3 Programmable grain boundary architectures. Deposition methods such as laser-induced crystallization and directed self-assembly now offer opportunities for deterministic grain boundary control. Cademartiri and Bishop reported on the concept of programmable self-assembly to design artificial grain boundary superlattices and twin-rich networks, providing a promising pathway for tunable charge transport in thin films.[115]

5.2.4 Low-dimensional and hybrid materials. Two-dimensional layered materials and hybrid perovskites offer new opportunities to mitigate trap states and carrier scattering at GBs owing to their atomically sharp interfaces and reduced defect density. Saidaminov et al. emphasized that low-dimensional halide perovskites and anisotropic SnSe structures exhibit enhanced carrier mobility by suppressing GB-related recombination.[116]

5.2.5 Scalable and sustainable processing. Aligning transport optimization with eco-friendly, scalable processing is a key challenge for commercialization. Recent advances using green solvents and room-temperature deposition for perovskite solar cells have demonstrated that defect healing and high performance can be achieved without compromising environmental sustainability, as highlighted by Miao et al.[117]

Taken together, these developments underscore that future innovation will depend on treating grain boundaries not as static defects but as programmable, chemically tunable features of polycrystalline semiconductors. By integrating advanced imaging, statistical modeling, boundary engineering, and sustainable processing, the field is positioned to achieve grain architectures with optimized carrier transport. This vision sets the stage for polycrystalline semiconductors to play a central role in next-generation optoelectronic, photovoltaic, and thermoelectric technologies.

6. Conclusions

This review establishes a unified framework connecting microscopic carrier transport theory with macroscopic electrical

23692 | J. Mater. Chem. C, 2025, 13, 23675–23695

This journal is © The Royal Society of Chemistry 2025

behavior in polycrystalline semiconductors. By integrating drift–diffusion, thermionic emission, tunneling, hopping, and shish–kebab conduction models with nanoscale experimental evidence, it clarifies how grain-boundary barriers, defect states, and crystallographic orientation collectively dictate charge mobility and recombination. The analysis demonstrates that grain boundaries are not merely performance-limiting defects but tunable electronic interfaces whose chemistry and structure can be engineered for enhanced functionality. Comparative insights from chalcogenide, oxide, and perovskite systems reveal that boundary passivation, dopant redistribution, and twin-boundary control can suppress non-radiative losses while promoting selective transport. Such findings underscore the transformative potential of grain-boundary engineering as a design strategy rather than a corrective process. Future advances will depend on coupling *in situ* and operando characterization with multiscale modeling to capture carrier dynamics under real device operation. Integrating data-driven approaches with atomic-level imaging could enable predictive design of grain architectures with programmable transport characteristics. By reframing grain boundaries as functional building blocks, this work outlines a roadmap toward high-mobility, high-stability polycrystalline semiconductors for next-generation optoelectronic, thermoelectric, and sensing technologies.

Author contributions

Israt Jahan: conceptualization, methodology, visualization, investigation, writing – original draft, writing – review and editing; Jesus Dustin Arellano: resources, writing- review, and editing; Zhisheng Shi: conceptualization, methodology, resources, supervision, writing – review and editing.

Conflicts of interest

The authors declare that they have no conflict of interest.

Data availability

This article is a review, and no new data were generated or analysed as part of this review. All data discussed are available in the cited literature.

Acknowledgements

Notes and references

1 H. F. Matare, *J. Appl. Phys.*, 1984, **56**, 2605–2631.

2 A. Kelly and K. M. Knowles, *Crystallography and crystal defects*, John Wiley & Sons, 2020.

3 K. Schulgasser, *J. Appl. Phys.*, 1976, **47**, 1880–1886.

4 J. Y. W. Seto, *J. Appl. Phys.*, 1975, **46**, 5247–5254.

5 X. Xiao, W. H. Li, Y. J. Fang, Y. Liu, Y. C. Shao, S. Yang, J. J. Zhao, X. Z. Dai, R. Zia and J. S. Huang, *Nat. Commun.*, 2020, **11**, 2215.

6 N. Nicoara, R. Manaligod, P. Jackson, D. Hariskos, W. Witte, G. Sozzi, R. Menozzi and S. Sadewasser, *Nat. Commun.*, 2019, **10**, 3980.

7 N. J. Jeon, H. Na, E. H. Jung, T. Y. Yang, Y. G. Lee, G. Kim, H. W. Shin, S. I. Seok, J. Lee and J. Seo, *Nat. Energy*, 2018, **3**, 682–689.

8 M. Jeong, I. W. Choi, E. M. Go, Y. Cho, M. Kim, B. Lee, S. Jeong, Y. Jo, H. W. Choi, J. Lee, J. H. Bae, S. K. Kwak, D. S. Kim and C. Yang, *Science*, 2020, **369**, 1615–1620.

9 F. Schindler, A. Fell, R. Müller, J. Benick, A. Richter, F. Feldmann, P. Krenckel, S. Riepe, M. C. Schubert and S. W. Glunz, *Sol. Energy Mater. Sol. Cells*, 2018, **185**, 198–204.

10 M. A. Scarpulla, B. McCandless, A. B. Phillips, Y. F. Yan, M. J. Heben, C. Wolden, G. Xiong, W. K. Metzger, D. Mao, D. Krasikov, I. Sankin, S. Grover, A. Munshi, W. Sampath, J. R. Sites, A. Bothwell, D. Albin, M. O. Reese, A. Romeo, M. Nardone, R. Klie, J. M. Walls, T. Fiducia, A. Abbas and S. M. Hayes, *Sol. Energy Mater. Sol. Cells*, 2023, **255**, 112289.

11 J. Keller, K. Kiselman, O. Donzel-Gargand, N. M. Martin, M. Babucci, O. Lundberg, E. Wallin, L. Stolt and M. Edoff, *Nat. Energy*, 2024, **9**, 467–478.

12 S. Ganguly, M. H. Jang, Y. H. Tan, S. S. Yoo, M. C. Gupta and A. W. Ghosh, *J. Appl. Phys.*, 2019, **126**, 143103.

13 M. S. Mahdi, K. Ibrahim, A. Hmood, N. M. Ahmed, S. A. Azzez and F. I. Mustafa, *RSC Adv.*, 2016, **6**, 114980.

14 Q. Lv, R. Li, L. Fan, Z. Huang, Z. Huan, M. Yu, H. Li, G. Liu, G. Qiao and J. Liu, *Sensors*, 2023, **23**, 8413.

15 S. Chen, H.-B. Li, Y. Fu, G.-Q. Liu, M. Ishaq, J. Luo, J.-M. Li, B. Che, J.-T. Luo, L. Ding, T. Chen and G.-X. Liang, *Nano Res.*, 2025, **18**, 94907159.

16 G. J. Snyder and E. S. Toberer, *Nat. Mater.*, 2008, **7**, 105–114.

17 J. W. Li, Z. J. Han, J. C. Yu, H. L. Zhuang, H. H. Hu, B. Su, H. Z. Li, Y. L. Jiang, L. Chen, W. S. Liu, Q. Zheng and J. F. Li, *Nat. Commun.*, 2023, **14**, 7428.

18 N. Yamazoe and K. Shimanoe, *Sens. Actuators, B*, 2008, **128**, 566–573.

19 S. Lee, Y. J. Cho, B. Han, J. Lee, S. Choi, T. Kang, H. Y. Chu, J. Kwag, S. C. Kim and J. Jang, *Adv. Eng. Mater.*, 2022, **24**, 2100910.

20 H. P. Komsa and A. V. Krasheninnikov, *Adv. Electron. Mater.*, 2017, **3**, 1600468.

21 H. Li, X. X. Liu, Y. S. Lin, B. Yang and Z. M. Du, *Phys. Chem. Chem. Phys.*, 2015, **17**, 11150–11155.

22 S. M. Sze and K. K. Ng, *Physics of Semiconductor Devices*, Wiley, New York, NY, USA, 3 edn, 2006.

23 D. M. Kim, A. N. Khondker, S. S. Ahmed and R. R. Shah, *IEEE Trans. Electron Devices*, 1984, **31**, 480–493.

This journal is © The Royal Society of Chemistry 2025

J. Mater. Chem. C, 2025, **13**, 23675–23695 | **23693**

24 J. C. M. Hwang, P. S. Ho, J. E. Lewis and D. R. Campbell, *J. Appl. Phys.*, 1980, **51**, 1576–1581.

25 C. H. Ling, *Solid State Electrochem.*, 1984, **27**, 633–638.

26 M. Santonen, A. Lahti, Z. J. Rad, M. Miettinen, M. Ebrahimzadeh, J. P. Lehtiö, E. Snellman, P. Laukkanen, M. Punkkinen, K. Kokko, K. Parkkinen and M. Eklund, *IEEE Trans. Electron Devices*, 2025, **72**, 1184–1190.

27 S. Schuler, S. Nishiwaki, J. Beckmann, N. Papathanasiou, S. Brehme, S. Siebentritt and M. Lux-Steiner, *Charge carrier transport in polycrystalline CuGaSe2 thin films*, 2002.

28 Y. Watanabe, *Annu. Rev. Mater. Sci.*, 1985, **15**, 71–98.

29 S. Husein, M. Stuckelberger, B. West, L. Ding, F. Dauzou, M. Morales-Masis, M. Duchamp, Z. Holman and M. I. Bertoni, *J. Appl. Phys.*, 2018, **123**, 245102.

30 J. U. Rahman, N. V. Du, W. H. Nam, W. H. Shin, K. H. Lee, W.-S. Seo, M. H. Kim and S. Lee, *Sci. Rep.*, 2019, **9**, 8624.

31 Q. Hao and J. Garg, *ES Mater. Manuf.*, 2021, **14**, 36–50.

32 S. Wang, S. Hui, K. L. Peng, T. P. Bailey, X. Y. Zhou, X. F. Tang and C. Uher, *J. Mater. Chem. C*, 2017, **5**, 10191–10200.

33 S. Park, M. A. Shehzad, M. F. Khan, G. Nazir, J. Eom, H. Noh and Y. Seo, *Carbon*, 2017, **112**, 142–148.

34 S. E. Krasavin and V. A. Osipov, *Sci. Rep.*, 2022, **12**, 14553.

35 E. Zuñiga-Puelles, A. Özden, R. Cardoso-Gil, C. Hennig, C. Himcinschi, J. Kortus and R. Gumeniuk, *J. Mater. Chem. A*, 2025, **13**, 9357–9371.

36 N. Sommer, J. Hüpkes and U. Rau, *Phys. Rev. Appl.*, 2016, **5**, 024009.

37 D. C. Hamilton, E. Arca, J. Pan, S. Siol, M. Young, S. Lany and A. Zakutayev, *J. Appl. Phys.*, 2019, **126**, 035701.

38 A. M. Ganose, J. Park, A. Faghaninia, R. Woods-Robinson, K. A. Persson and A. Jain, *Nat. Commun.*, 2021, **12**, 2222.

39 J. Shuai, J. Mao, S. W. Song, Q. Zhu, J. F. Sun, Y. M. Wang, R. He, J. W. Zhou, G. Chen, D. J. Singh and Z. F. Ren, *Energy Environ. Sci.*, 2017, **10**, 799–807.

40 Y. P. Wang, S. G. Sun, Y. A. Huang, Y. Fu, J. N. Qi, K. Tie, Z. W. Wang, F. Jiao, R. M. Si, X. S. Chen, L. Q. Li and W. P. Hu, *Aggregate*, 2023, **4**, e379.

41 J. Quirk, M. Rothmann, W. Li, D. Abou-Ras and K. P. McKenna, *Appl. Phys. Rev.*, 2024, **11**, 011308.

42 T. Katase, S. Nomoto, X. He, S. Kitani, T. Honda, H. Hiramatsu, H. Hosono and T. Kamiya, *ACS Appl. Electron. Mater.*, 2024, **6**, 7424–7429.

43 B. Gaury and P. M. Haney, *Phys. Rev. Appl.*, 2017, **8**, 054026.

44 A. Cuevas and D. Macdonald, *Sol. Energy*, 2004, **76**, 255–262.

45 W. K. Metzger, I. L. Repins, M. Romero, P. Dippo, M. Contreras, R. Noufi and D. Levi, *Thin Solid Films*, 2009, **517**, 2360–2364.

46 J. Wong, J. L. Huang, S. Varlamov, M. A. Green and M. Keevers, *Prog. Photovoltaics*, 2012, **20**, 915–922.

47 T. Fuyuki, H. Kondo, T. Yamazaki, Y. Takahashi and Y. Uraoka, *Appl. Phys. Lett.*, 2005, **86**, 262108.

48 X. Yang, Y. Fu, R. Su, Y. Zheng, Y. Zhang, W. Yang, M. Yu, P. Chen, Y. Wang, J. Wu, D. Luo, Y. Tu, L. Zhao, Q. Gong and R. Zhu, *Adv. Mater.*, 2020, **32**, 2002585.

49 Z. Gao, C. Leng, H. Zhao, X. Wei, H. Shi and Z. Xiao, *Adv. Mater.*, 2023, **36**, 2304855.

50 Y. Kajikawa, *J. Appl. Phys.*, 2013, **114**, 043719.

51 N. C. Lu, L. Gerzberg, C. Y. Lu and J. D. Meindl, *IEEE Trans. Electron Devices*, 1983, **30**, 137–149.

52 E. L. Murphy and R. H. Good, *Phys. Rev.*, 1956, **102**, 1464–1473.

53 D. K. Schroder, *Semiconductor Material and Device Characterization*, Wiley, 3rd edn, 2006.

54 N. Cifuentes, S. Ghosh, A. Shongolova, M. R. Correia, P. M. P. Salomé, P. A. Fernandes, S. Ranjbar, S. Garud, B. Vermang, G. M. Ribeiro and J. C. González, *J. Phys. Chem. C*, 2020, **124**, 7677–7682.

55 J. C. Slater, *Phys. Rev.*, 1956, **103**, 1631–1644.

56 Y. D. Zhang, J. X. Zuo, P. J. Li, Y. H. Gao, W. W. He and Z. Zheng, *Physica E*, 2019, **111**, 75–78.

57 B. Bahrami, S. Mabrouk, N. Adhikari, H. Elbohy, A. Gurung, K. M. Reza, R. Pathak, A. H. Chowdhury, G. Saianand, W. J. Yue, J. T. Zai, X. F. Qian, M. Liang and Q. Q. Qiao, *InfoMat*, 2020, **2**, 409–423.

58 J. S. Yun, J. Seidel, J. Kim, A. M. Soufiani, S. J. Huang, J. Lau, N. J. Jeon, S. I. Seok, M. A. Green and A. Ho-Baillie, *Adv. Energy Mater.*, 2016, **6**, 1600330.

59 C. Li, Y. L. Wu, J. Poplawsky, T. J. Pennycook, N. Paudel, W. J. Yin, S. J. Haigh, M. P. Oxley, A. R. Lupini, M. Al-Jassim, S. J. Pennycook and Y. F. Yan, *Phys. Rev. Lett.*, 2014, **112**, 156103.

60 P. R. Edwards, S. A. Galloway and K. Durose, *Thin Solid Films*, 2000, **372**, 284–291.

61 L. X. Zhang, J. L. F. Da Silva, J. B. Li, Y. F. Yan, T. A. Gessert and S. H. Wei, *Phys. Rev. Lett.*, 2008, **101**, 155501.

62 X. J. Ma, F. Zhang, Z. D. Chu, J. Hao, X. H. Chen, J. M. Quan, Z. Y. Huang, X. M. Wang, X. Q. Li, Y. F. Yan, K. Zhu and K. J. Lai, *Nat. Commun.*, 2021, **12**, 5009.

63 J. J. Kuo, S. D. Kang, K. Imasato, H. Tamaki, S. Ohno, T. Kanno and G. J. Snyder, *Energy Environ. Sci.*, 2018, **11**, 429–434.

64 R. G. Forbes, *R. Soc. Open Sci.*, 2019, **6**, 190912.

65 D. Z. Chen, R. Jacobs, J. Petillo, V. Vlahos, K. L. Jensen, D. Morgan and J. Booske, *Phys. Rev. Appl.*, 2022, **18**, 054010.

66 S. K. Kolekar, R. V. Godbole, V. P. Godbole and C. V. Dharmadhikari, *AIP Adv.*, 2020, **10**, 045129.

67 W. Li, K. Nomoto, D. Jena and H. G. Xing, *Appl. Phys. Lett.*, 2020, **117**, 222104.

68 C. B. Lin, J. D. Chen and Y. Y. Fu, *Appl. Phys. Lett.*, 2024, **124**, 074103.

69 V. H. Nguyen, U. Gottlieb, A. Valla, D. Muñoz, D. Bellet and D. Muñoz-Rojas, *Mater. Horiz.*, 2018, **5**, 715–726.

70 K. Sharma and D. P. Joshi, *J. Appl. Phys.*, 2009, **106**, 024504.

71 Z. Dashevsky, V. Kasiyan, G. Radovsky, E. Shufer and M. Auslender, *Proc. SPIE*, 2008, **7142**, DOI: 10.1117/12.815199.

72 F. P. Garcia de Arquer, X. Gong, R. P. Sabatini, M. Liu, G. H. Kim, B. R. Sutherland, O. Voznyy, J. Xu, Y. Pang, S. Hoogland, D. Sinton and E. Sargent, *Nat. Commun.*, 2017, **8**, 14757.

23694 | *J. Mater. Chem. C*, 2025, **13**, 23675–23695

This journal is © The Royal Society of Chemistry 2025

73 W. Su, N. Kumar, H. Shu, O. Lancry and M. Chaigneau, *J. Phys. Chem. C*, 2021, **125**, 26883–26891.

74 N. F. Mott, *J. Non-Cryst. Solids*, 1968, **1**, 1–17.

75 B. I. Shklovskii and A. L. Efros, *Electronic Properties of Doped Semiconductors*, Springer, Berlin, Heidelberg, 1984.

76 D. Yu, C. J. Wang, B. L. Wehrenberg and P. Guyot-Sionnest, *Phys. Rev. Lett.*, 2004, **92**, 216802.

77 C. C. Hsu, C. H. Chou, W. C. Jhang and P. T. Chen, *Physica B*, 2019, **569**, 80–86.

78 A. A. Dobrovolsky, Z. M. Dashevsky, V. A. Kasiyan, L. I. Ryabova and D. R. Khokhlov, *Semicond. Sci. Technol.*, 2009, **24**, 075010.

79 B. Mahapatra and S. Sarkar, *Heliyon*, 2022, **8**, e10961.

80 R. Rahman and J. A. Scales, *Appl. Phys. Lett.*, 2016, **109**, 092103.

81 C. Guillen and J. Herrero, *J. Appl. Phys.*, 1992, **71**, 5479–5484.

82 J. J. Wang, J. S. Bi, G. B. Xu and M. X. Liu, *Electronics*, 2024, **13**, 1427.

83 L. H. Zhao, J. J. Qiu, B. B. Weng, C. Chang, Z. J. Yuan and Z. S. Shi, *J. Appl. Phys.*, 2014, **115**, 084502.

84 M. Rastkar Mirzaei and Z. Shi, *Appl. Phys. Lett.*, 2024, **125**, 083501.

85 B. Weng, J. Qiu, L. Zhao, Z. Yuan, C. Chang and Z. Shi, *SPIE Proc.*, 2013, **8993**, 899311.

86 G. Hahn, M. Käs and B. Herzog, *Solid State Phenom.*, 2010, **156–158**, 343–349.

87 N. H. Nickel, *Solid State Phenom.*, 2010, **156–158**, 351–356.

88 X. X. Wen, Z. H. Lu, X. K. Yang, C. Chen, M. A. Washington, G. C. Wang, J. Tang, Q. Zhao and T. M. Lu, *ACS Appl. Mater. Interfaces*, 2023, **15**, 22251–22262.

89 S. Han and A. J. Flewitt, *Thin Solid Films*, 2020, **704**, 138000.

90 M. Birkholz, B. Selle, F. Fenske and W. Fuhs, *Phys. Rev. B: Condens. Matter Mater. Phys.*, 2003, **68**, 205414.

91 X. Y. Li, Y. S. Du, K. Y. Yang, S. K. Li, J. Y. Zhang, L. Li, J. J. Xing, G. H. Rao, J. T. Zhao and K. Guo, *Adv. Funct. Mater.*, 2025, e12586.

92 C. Hu, K. Xia, C. Fu, X. Zhao and T. Zhu, *Energy Environ. Sci.*, 2022, **15**, 1406–1422.

93 T. H. Ly, D. J. Perello, J. Zhao, Q. M. Deng, H. Kim, G. H. Han, S. H. Chae, H. Y. Jeong and Y. H. Lee, *Nat. Commun.*, 2016, **7**, 10426.

94 M. Yang, Y. Zeng, Z. Li, D. H. Kim, C.-S. Jiang, J. van de Lagemaat and K. Zhu, *Phys. Chem. Chem. Phys.*, 2017, **19**, 5043–5050.

95 M. S. Hammer, D. Rauh, V. Lorrmann, C. Deibel and V. Dyakonov, *Nanotechnology*, 2008, **19**, 485701.

96 J. Sengupta, R. K. Sahoo and C. D. Mukherjee, *Mater. Lett.*, 2012, **83**, 84–87.

97 S. F. Varol, D. Sahin, M. Kompitsas and G. Çankaya, *RSC Adv.*, 2014, **4**, 13593–13600.

98 H. Bishara, S. Lee, T. Brink, M. Ghidelli and G. Dehm, *ACS Nano*, 2021, **15**, 16607–16615.

99 R. E. Williams, Q. M. Ramasse, K. P. McKenna, L. J. Phillips, P. J. Yates, O. S. Hutter, K. Durose, J. D. Major and B. G. Mendis, *ACS Appl. Mater. Interfaces*, 2020, **12**, 21730–21738.

100 A. Broniatowski, *Phys. Rev. B: Condens. Matter Mater. Phys.*, 1987, **36**, 5895–5905.

101 M. J. Watts, P. Hatton, R. Smith, T. Fiducia, A. Abbas, R. Greenhalgh, J. M. Walls and P. Goddard, *Phys. Rev. Mater.*, 2021, **5**, 035403.

102 J. Moseley, M. M. Al-Jassim, H. L. Guthrey, J. M. Burst, J. N. Duenow, R. K. Ahrenkiel and W. K. Metzger, *J. Appl. Phys.*, 2016, **120**, 105704.

103 W. Zheng, Y. N. Zhang and J. Q. Tian, *Chalcogenide Lett.*, 2017, **14**, 275–281.

104 W. S. Cai, Z. G. Zang and L. M. Ding, *J. Semicond.*, 2021, **42**, 030203.

105 P. Xiao, L. F. Lan, T. Dong, Z. G. Lin, W. Shi, R. H. Yao, X. H. Zhu and J. B. Peng, *Appl. Phys. Lett.*, 2014, **104**, 051607.

106 S. Wang, V. Mirkhani, K. Yapabandara, R. Cheng, G. Hernandez, M. P. Khanal, M. S. Sultan, S. Uprety, L. Shen, S. Zou, P. Xu, C. D. Ellis, J. A. Sellers, M. C. Hamilton, G. Niu, M. H. Sk and M. Park, *J. Appl. Phys.*, 2018, **123**, 161503.

107 J. S. Huang and C. F. Lin, *J. Appl. Phys.*, 2008, **103**, 014304.

108 S. Q. Cai, Y. M. Li, X. Chen, Y. Y. Ma, X. J. Liu and Y. Q. He, *J. Mater. Sci.: Mater. Electron.*, 2016, **27**, 6166–6174.

109 I. T. Lu, J. J. Zhou, J. Park and M. Bernardi, *Phys. Rev. Mater.*, 2022, **6**, L010801.

110 K. C. Kim, J. Lee, B. K. Kim, W. Y. Choi, H. J. Chang, S. O. Won, B. Kwon, S. K. Kim, D. B. Hyun, H. J. Kim, H. C. Koo, J. H. Choi, D. I. Kim, J. S. Kim and S. H. Baek, *Nat. Commun.*, 2016, **7**, 12449.

111 P. Barathieu, B. Caussat, E. Scheid, D. Jaume and J. P. Couderc, *J. Electrochem. Soc.*, 2001, **148**, C149–C155.

112 Y. Do, D. Y. Jeong, S. Lee, S. Kang, S. Jang and J. Jang, *Adv. Eng. Mater.*, 2020, **22**, 1901430.

113 Y. T. Liu, J. H. Yang, B. J. Lawrie, K. P. Kelley, M. Ziatdinov, S. V. Kalinin and M. Ahmadi, *ACS Nano*, 2023, **17**, 9647–9657.

114 Z. R. He, S. Bi and K. Asare-Yeboah, *Coatings*, 2025, **15**, 164.

115 L. Cademartiri and K. J. M. Bishop, *Nat. Mater.*, 2015, **14**, 2–9.

116 M. I. Saidaminov, O. F. Mohammed and O. M. Bakr, *ACS Energy Lett.*, 2017, **2**, 889–896.

117 Y. F. Miao, M. Ren, Y. T. Chen, H. F. Wang, H. R. Chen, X. M. Liu, T. F. Wang and Y. X. Zhao, *Nat. Sustain.*, 2023, **6**, 1465–1473.

This journal is © The Royal Society of Chemistry 2025

J. Mater. Chem. C, 2025, **13**, 23675–23695 | **23695**